I&EC research
Industrial & Engineering Chemistry Research

pubs.acs.org/IECR
Article

Surrogate-Assisted Optimization for Real-World Wet-Process Phosphoric Acid Production

Zixuan Zhang, Xiaowei Song, Yujiao Zeng,* Jianhua Chen, Limin Wang, Songlin Liu, Shaoxiu Xue, Zhiwu Zhou, Jie Li, and Xin Xiao*

Cite This: *Ind. Eng. Chem. Res.* 2025, 64, 24138−24155

ABSTRACT: Wet-process phosphoric acid production (WPAP) is a crucial part of modern industry, and its optimization can enhance production efficiency and enable precise utilization of ore resources. However, due to the complexity of its reaction mechanisms, effective simulation and optimization methods remain lacking. To address these issues, this study integrates lab-scale kinetic models, which are based on both the literature and industrial data, into full-process simulation to construct a precise first-principles model. By combining the first-principles model with actual production data, an accurate and computationally efficient surrogate model is established. Three optimization scenarios were developed based on real-world conditions, aiming to minimize the content of nonwater-soluble phosphorus (NWSP). The sequential quadratic programming for machine learning-embedded optimization (MLSQP) algorithm was applied to solve these optimization problems, enabling efficient convergence to the Karush−Kuhn−Tucker (KKT) point of the surrogate model. Validated by the rigorous model, the optimizations under the three scenarios achieved reductions of 20.79%, 8.91%, and 38.61% in NWSP, respectively. Field tests confirmed an 8.3% reduction in total residual phosphorus and an 8.9% decrease in NWSP, without an increase in energy or raw material consumption.

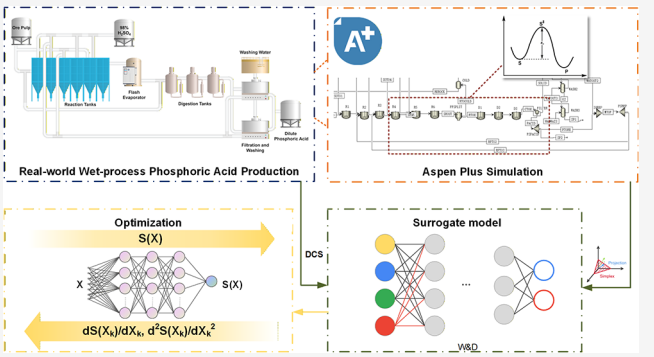

1. INTRODUCTION

Phosphorus serves as the lifeline of modern agriculture[1,2] and stands as a cornerstone of contemporary industry.[3] Phosphorus is widely used in manufacturing fertilizers,[4,5] food production,[6] semiconductors,[7] batteries,[8] and so on. With the development of science and technology, the demand for phosphorus-containing chemicals is increasing.[9,10] In industrial processes, the primary methods for extracting phosphorus from these ores are the wet process[8,11−13] and the thermal process.[14−16] Although phosphoric acid produced by the thermal process contains less fluorine and is purer,[14,17] 85−95% of phosphoric acid is produced through wet process[17,18] due to its affordability and low energy consumption.[19]

However, wet-process phosphoric acid production (WPAP) suffers from phosphorus loss. The phosphorus loss in WPAP is mainly in the form of nonwater-soluble phosphorus, including unreacted fluorapatite, calcium hydrogen phosphate dihydrate ($CaHPO_4{\cdot}2H_2O$) crystals, and metal phosphate crystals. Many researchers have conducted extensive experiments and developed kinetic models specifically for phosphate rock dissolution and phosphogypsum precipitation. Some researchers focus on developing a conversion-based empirical kinetic model for the acidulation of phosphate rock,[20−22] taking into account various factors, including liquid-to-solid ratio, acid concentration, particle size distribution, stirring rate, temperature, and residence time. Research on the precipitation of phosphogypsum has primarily concentrated on developing solubility models under different P_2O_5, SO_3 concentration, as well as temperature.[23−26] Abutayeh and Campbell[23] employed the Edwards−Maurer−Newman−Prausnitz Pitzer-based model to predict P_2O_5 loss. Dorozhkin[27,28] studied the dissolution process of natural single fluorophosphate crystals in phosphoric acid solution, and the measured dissolution rate was applied to computer simulation of industrial reactors. For the concentration section, Joao et al.[29] conducted dynamic simulation. Nevertheless, the existing kinetic studies and process modeling efforts have been conducted independently without integration into industrial-scale WPAP simulations. This disconnect makes lab-scale models fail to capture the inherent variability of industrial environments. Therefore, one

Received: August 8, 2025
Revised: November 20, 2025
Accepted: November 26, 2025
Published: December 6, 2025

https://doi.org/10.1021/acs.iecr.5c03286
Ind. Eng. Chem. Res. 2025, 64, 24138−24155

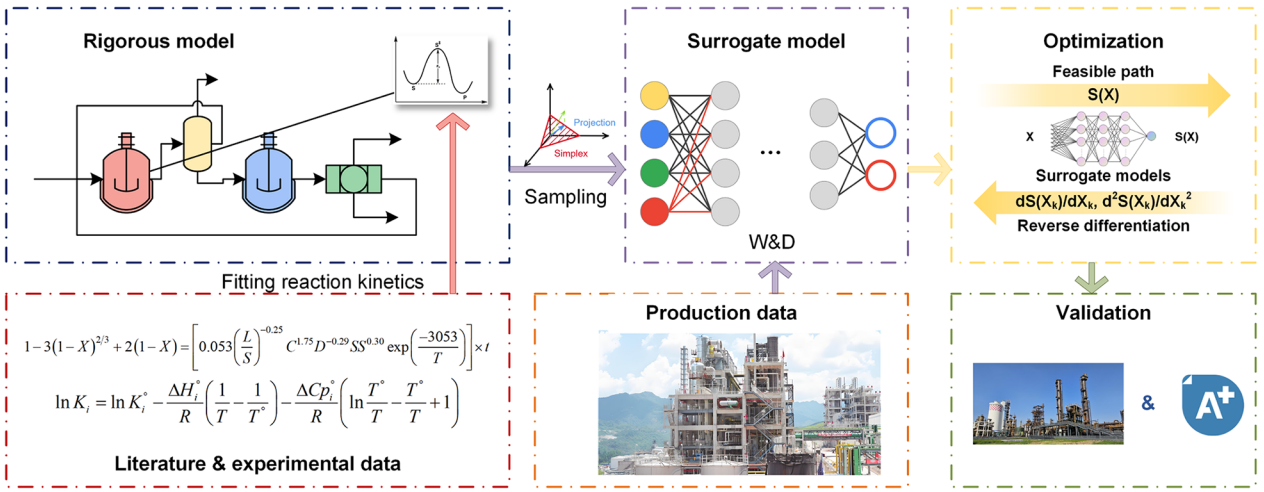

Figure 1. Framework of surrogate-assisted optimization of real-world WPAP.

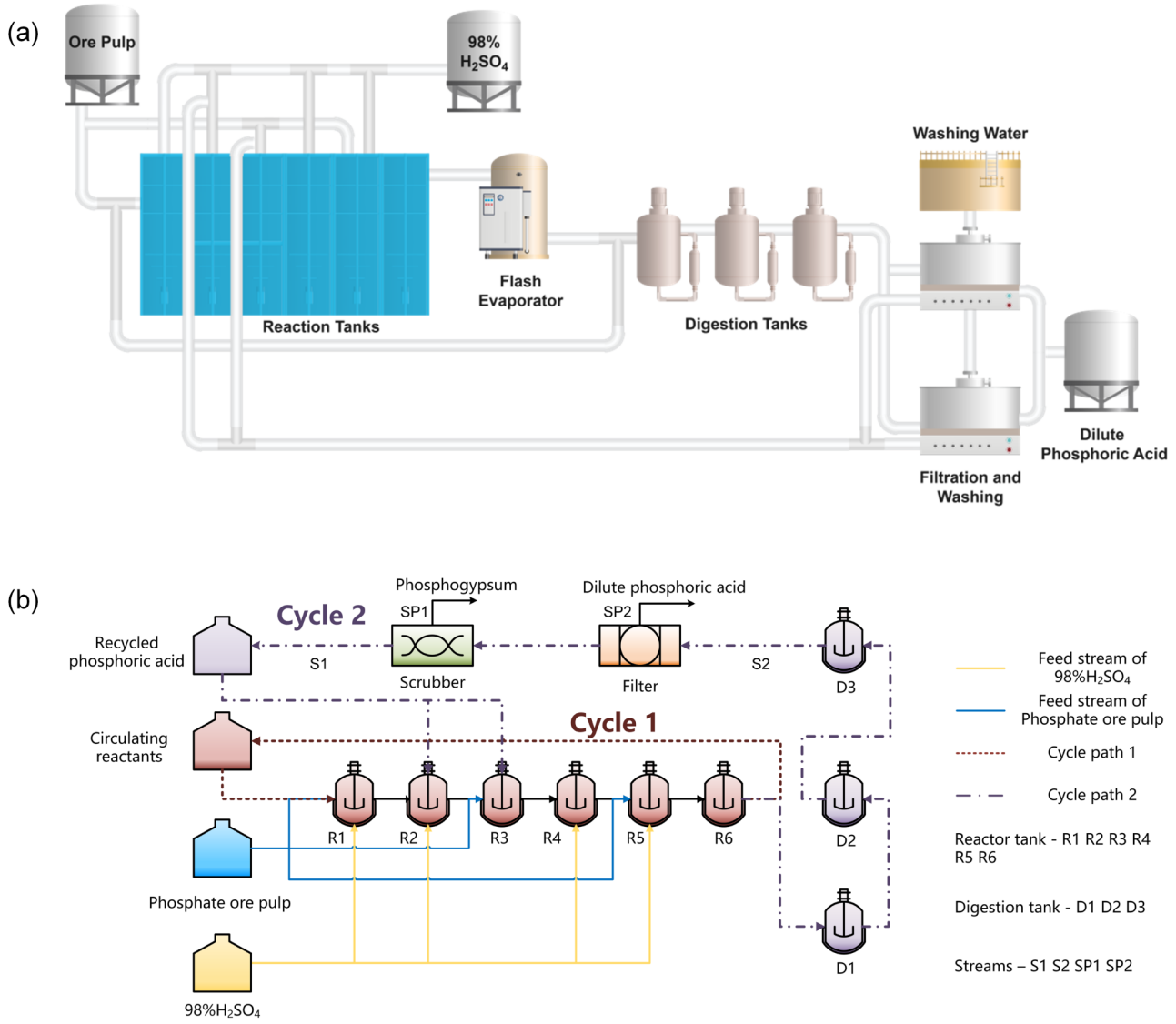

Figure 2. (a) Real-world wet phosphoric acid production process and (b) its simplified process flow diagram.

motivation for this work is to incorporate lab-scale kinetic models into industrial-scale models.

With the development of machine learning techniques, data-driven methods have emerged as an additional and promising alternative for modeling, aiming to narrow the gap between

https://doi.org/10.1021/acs.iecr.5c03286
Ind. Eng. Chem. Res. 2025, 64, 24138−24155

mechanistic models and actual production. Elmisaoui et al.[30] developed a hierarchical sparse polynomial interpolation for the first-principle model of phosphate ore dissolution.[31] Bouchkira et al.[32] delveloped a surrogate model based on industrial data for validating the solutionsobtained from first-principle model-based optimization. However, industrial data are usually collected under stable operating conditions and thus tend to cluster around nominal values, lacking a uniform distribution. In contrast, data generated by first-principles models can offer more evenly distributed samples, but they may not fully reflect the complexity and variability of the actual production processes. Therefore, in this work, we integrate both data sources for building a model that conforms to actual production and has a strong generalization ability.

Once the prediction model is established, optimization techniques[33,34] can be used to find the operating conditions that minimize nonwater-soluble phosphorus (NWSP). Cho et al.[35] conducted a process simulation for WPAP with hemihydrate phosphogypsum and conducted a sensitivity analysis to increase the concentration of phosphoric acid. Bouchkira et al.[32] established a simulation model for a phosphoric acid dissolution tank based on mass and energy balance and applied it to an industrial multiobjective optimization problem. Bojarski et al.[36] combined life cycle optimization with process simulation under uncertainty to reduce pollution in wet-process phosphoric acid production. However, to more easily solve the optimization problem, the aforementioned studies rely solely on mass and energy balances or are limited to simplified empirical thermodynamic models. This leads to limited accuracy in full-process simulations, thereby making them unsuitable for meeting the optimization requirements of a more refined production. Therefore, the ultimate goal of this work is to incorporate well-designed models into the optimization problem and propose a time-saving optimization algorithm.

In this work, as illustrated in Figure 1, we present an advanced modeling method for WPAP by integrating a process simulation with a precise kinetic model. This approach is capable of developing a high-fidelity surrogate, which combines simulated data with real-world operational data. To address the challenges of optimizing complex chemical processes using surrogate models, we propose the sequential quadratic programming for machine learning-embedded optimization (MLSQP) algorithm. Compared to commonly used heuristic methods such as genetic algorithms (GA) and particle swarm optimization (PSO), the MLSQP algorithm demonstrates superior convergence and stability, allowing rapid convergence to the Karush−Kuhn−Tucker (KKT) point. Furthermore, the proposed framework has been successfully implemented in an industrial setting, resulting in significant improvements in both production efficiency and environmental performance. These results not only validate the effectiveness of the approach but also establish a replicable paradigm for optimizing other complex chemical systems. The main contributions of this work are summarized as follows:

1) A first-principles model is developed by integrating a lab-scale kinetic model with plant-scale process simulation. Based on this mechanistic model and real-world operational data, an accurate surrogate model for WPAP is established.

2) The MLSQP algorithm is proposed for solving surrogate-assisted optimization problems, enabling fast and stable convergence to the KKT point.

2. PROBLEM STATEMENT

2.1. Process Description. A real-world wet phosphoric acid production process is illustrated in Figure 2. The entire process contains sections including attack and digestion reactors, flash coolers, filtration, and washing units.

In the real-world process shown in Figure 2(a), the reactor is divided into 6 subtanks, corresponding to R1−R6, as shown in Figure 2(b), where the acid attack reaction of fluorapatite and impurity metal oxides mainly occurs, and partial gypsum and NWSP crystals are also formed. Passing through the reaction tank, most of the materials enter flash cooling and are circulated back to the reactor from tank 1 for complete reaction. The material overflowing from the upper layer of the reactor enters 3 consecutive digestion tanks, corresponding to D1−D3 for more complete crystallization. Subsequently, the materials enter two filtration series, which are simplified using a single filtration unit coupled with a three-effect wash system. The filtrate is dilute phosphoric acid (SP2); after washing, the filter cake becomes phosphogypsum (SP1), and the washed water enters R2 and R3 as recycled phosphoric acid. The phosphate ore pulp streams are fed into subtanks R1, R3, and R5, and the sulfuric acid streams are fed into subtanks R1, R2, R4, and R5. In practical production, this novel feeding method aids in precisely managing the concentrations of SO_3 and P_2O_5, ensuring strict control over gypsum crystallization within the dihydrate zone and promoting a more favorable crystalline morphology for washing. The main raw materials for this process are concentrated sulfuric acid (98% H_2SO_4) and phosphate ore pulp. The ore composition, particle size distribution data, and main reactions are shown in Supporting Information.

2.2. Optimization Problems Description. The efficiency and economy of the production system are determined by the residual total phosphorus in gypsum. Total phosphorus includes water-soluble phosphorus and NWSP. The residual amount of water-soluble phosphorus is mainly influenced by the crystal morphology of gypsum. Flake-shaped dihydrate gypsum crystals are more conducive to thorough washing, thereby helping to reduce water-soluble phosphorus, whereas needle-shaped crystals have the opposite effect. Notably, the crystal morphology of gypsum is controlled by the concentrations of SO_3 and P_2O_5 in the digestion tank. Therefore, once we control the concentrations of SO_3 and P_2O_5 in the digestion tank, the residual water-soluble phosphorus can be stabilized. For NWSP, primarily including phosphorus in unreacted ore and metal phosphate crystals, its final content is related to the local concentrations of SO_3 and P_2O_5 in each reaction tank.

Based on real-world production experience, once the feed ratio of total sulfuric acid to ore pulp and the amount of washing water are determined, the concentrations of SO_3 and P_2O_5 in the digestion tank can be kept relatively stable, which in turn stabilizes the residual soluble phosphorus in gypsum. Therefore, the optimization models are proposed to reduce the residual NWSP in gypsum under a fixed ore-acid ratio and washing water. This goal is achieved by adjusting the local concentrations of SO_3 and P_2O_5 in each reaction tank, and this

https://doi.org/10.1021/acs.iecr.5c03286
Ind. Eng. Chem. Res. 2025, 64, 24138−24155

adjustment is accomplished by regulating the feed ratio of sulfuric acid/ore pulp in each reaction tank.

We considered three optimization scenarios. The first one is to minimize the NWSP under the current production conditions. The second goal is to maximize the system capacity while maintaining or reducing the content of NWSP. The third goal is a design-oriented problem. For a system with two new reaction tanks added, which means the capacity will be increased, minimize its NWSP. The process flow diagram of scenario 3 is shown in Figure S1 in Supporting Information. The decision variables for the three scenarios are all the feed ratios of sulfuric acid and ore pulp in each reaction tank, while the decision variables for Scenario 2 also include the total feed load.

2.2.1. Scenario 1: Minimize NWSP of Base Process. In scenario 1, the objective, as shown in eq 1, is to minimize the mass fraction of nonsoluble phosphorus in SP1 by only adjusting the ratio of sulfuric acid and ore pulp fed to each reaction tank.

$$\min_{\mathbf{x}\in\mathbb{R}^4,\,\mathbf{y}\in\mathbb{R}^3} \quad \mathrm{MF}_{\mathrm{SP1}}^{\mathrm{NP}} \tag{1}$$

The phosphorus atom conservation is used to calculate the content of P_2O_5. The equation is as follows:

$$\mathrm{MF}^{\mathrm{NP}} = \frac{M(\mathrm{P_2O_5})}{2} \times \sum_{i\in\mathrm{NSP}} \frac{N^i \times \mathrm{MF}^i}{M(i)} \tag{2}$$

Where i represents the components containing phosphorus element, $M(\cdot)$ is the relative molecular weight, and N is the number of phosphorus atoms in the molecular formula.

The decision variables $\mathbf{x}$ and $\mathbf{y}$, upon being input into the simulator or surrogate model for computation, yield the corresponding values of the state variables, as shown in eq 3.

$$F_1(\mathbf{x}, \mathbf{y}) = [\mathrm{MF}_{\mathrm{SP1}}^{\mathrm{NP}}, \mathrm{MF}_{\mathrm{SP2}}^{\mathrm{P}}] \tag{3}$$

Where $\mathbf{x}$ represents the ratio of sulfuric acid fed into R1, R2, R4, and R5; and $\mathbf{y}$ represents the ratio of ore pulp fed into R1, R3, R5; $F_1(\cdot)$ represents the simulator or surrogate model for the process system shown in Figure 2(b).

In addition, production limitations necessitate the introduction of several additional constraints. The feed ratio should follow the normalization equation, as shown in eq 4 and eq 5.

$$1_4\mathbf{x} = 1 \tag{4}$$

$$1_3\mathbf{y} = 1 \tag{5}$$

Our reaction hypothesis is valid only if the concentration of phosphoric acid is controlled within the dihydrate crystallization range. Therefore, it is essential to restrict the concentration of dilute phosphoric acid accordingly:

$$24 \le \mathrm{MF}_{\mathrm{SP2}}^{\mathrm{P}} \le 26 \tag{6}$$

The maximum flow rate of the pipeline, the temperature of the reactor, and the uniformity of the feed require setting upper and lower bounds on the proportion entering reactors, as shown in eq 7 and eq 8.

$$\mathbf{x}_1^{\mathrm{lb}} \le \mathbf{x} \le \mathbf{x}_1^{\mathrm{ub}} \tag{7}$$

$$\mathbf{y}_1^{\mathrm{lb}} \le \mathbf{y} \le \mathbf{y}_1^{\mathrm{ub}} \tag{8}$$

Where in scenario 1, $\mathbf{x}_1^{\mathrm{lb}} = [0.08, 0.1, 0.1, 0.08]$ and $\mathbf{x}_1^{\mathrm{ub}} = [0.21, 1, 1, 0.11]$ are the lower and upper bounds of ratio of sulfuric acid fed into R1, R2, R4, and R5, respectively; and $\mathbf{y}_1^{\mathrm{lb}} = [0.1, 0.1, 0.08]$ and $\mathbf{y}_1^{\mathrm{ub}} = [1, 1, 0.12]$ are the lower and upper bounds of ratio of ore pulp fed into R1, R3, and R5, respectively.

2.2.2. Scenario 2: Maximize Load of Base Process While Keeping NWSP Constant. In scenario 2, we aim to investigate the maximum system load under the condition of maintaining or reducing NWSP. This optimization seeks to improve the system capacity and production efficiency. The objective is shown in eq 9:

$$\min_{\mathbf{x}\in\mathbb{R}^4,\,\mathbf{y}\in\mathbb{R}^3,\,l\in\mathbb{R}} \quad -l + \mathrm{MF}_{\mathrm{SP1}}^{\mathrm{NP}} \tag{9}$$

Accordingly, the simulator or the surrogate model should be

$$F_2(\mathbf{x}, \mathbf{y}, l) = [\mathrm{MF}_{\mathrm{SP1}}^{\mathrm{NP}}, \mathrm{MF}_{\mathrm{SP2}}^{\mathrm{P}}] \tag{10}$$

Where l is the factor by which the load is increased, ranging from 1 to 1.15:

$$1 \le l \le 1.15 \tag{11}$$

Equations 4−8 are also taken as the constraints in this optimization problem.

2.2.3. Scenario 3: Minimize NWSP of Revamped Process. Scenario 3 is a design-oriented problem focused on enhancing the production system. Two new reaction tanks, RN1 and RN2, were added between R3 and R4. Given the system's structure and load, this optimization aims to adjust the branching ratio of the feed to achieve the minimum NWSP content. The objective was as follows:

$$\min_{\mathbf{x}\in\mathbb{R}^5,\,\mathrm{y}\in\mathbb{R}^4} \quad \mathrm{MF}_{\mathrm{SP1}}^{\mathrm{NP}} \tag{12}$$

Similarly, we have

$$F_3(\mathbf{x}, \mathbf{y}) = [\mathrm{MF}_{\mathrm{SP1}}^{\mathrm{NP}}, \mathrm{MF}_{\mathrm{SP2}}^{\mathrm{P}}] \tag{13}$$

Where $\mathbf{x}$ represents the ratio of sulfuric acid fed into R1, R2, R4, R5, and RN2, and $\mathbf{y}$ represents the ratio of ore pulp fed into R1, R3, R5, and RN1; $F_3(\cdot)$ represents the simulator or surrogate model for the upgraded production system. Equation 6 is also taken as a constraint in this optimization problem.

Besides, the normalization equation should be

$$1_5\mathbf{x} = 1 \tag{14}$$

$$1_4\mathbf{y} = 1 \tag{15}$$

The constraints to feed ratio are

$$\mathbf{x}_3^{\mathrm{lb}} \le \mathbf{x} \le \mathbf{x}_3^{\mathrm{ub}} \tag{16}$$

$$\mathbf{y}_3^{\mathrm{lb}} \le \mathbf{y} \le \mathbf{y}_3^{\mathrm{ub}} \tag{17}$$

Where $\mathbf{x}_3^{\mathrm{lb}} = [0.08, 0.1, 0.1, 0.08, 0.2]$ and $\mathbf{x}_1^{\mathrm{ub}} = [0.21, 1, 1, 0.11, 0.4]$ are the lower and upper bounds of ratio of sulfuric acid fed into R1, R2, R4, R5, and RN2, respectively, and $\mathbf{y}_3^{\mathrm{lb}} = [0.1, 0.1, 0.08, 0.2]$ and $\mathbf{y}_3^{\mathrm{ub}} = [1, 1, 0.12, 0.4]$ are the lower and upper bounds of ratio of ore pulp fed into R1, R3 R5, and RN1, respectively.

3. METHODOLOGY

In this section, a workflow of surrogate-assisted hybrid modeling and optimization methodology is proposed, as shown in Figure 3. We first establish a full-process mass and

https://doi.org/10.1021/acs.iecr.5c03286
Ind. Eng. Chem. Res. 2025, 64, 24138−24155

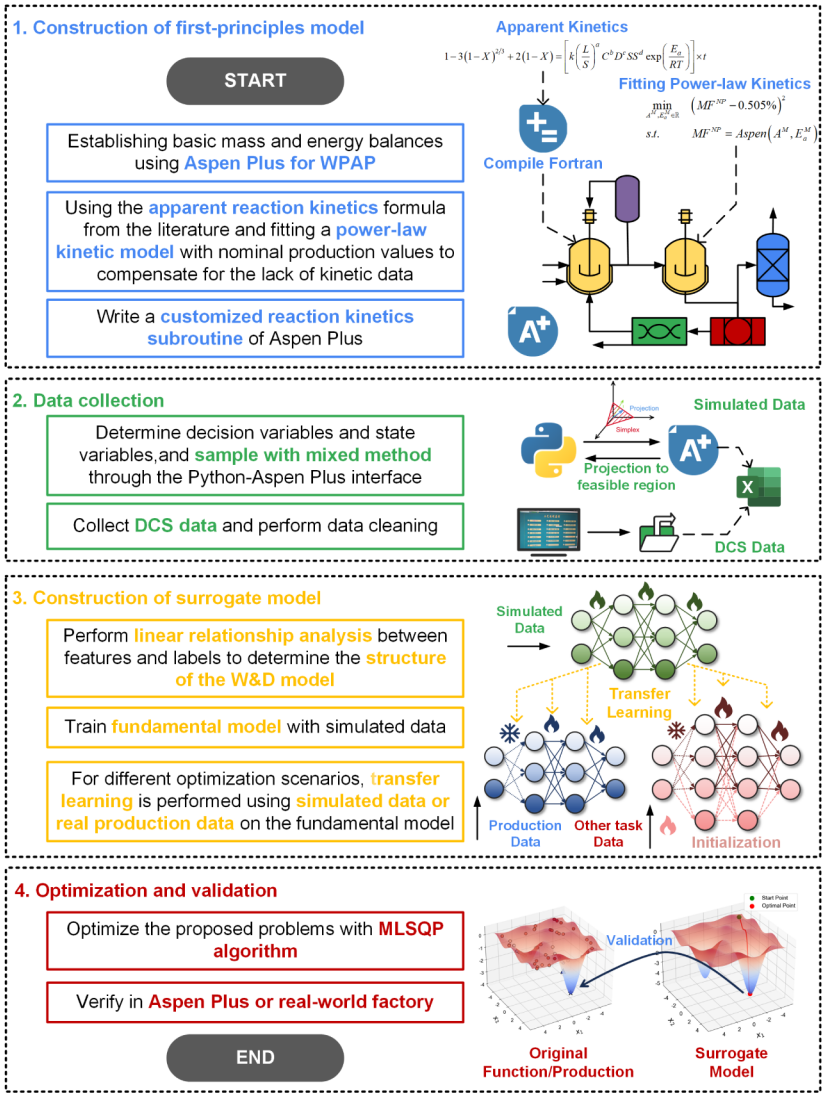

Figure 3. Workflow of surrogate-assisted hybrid modeling and optimization methodology.

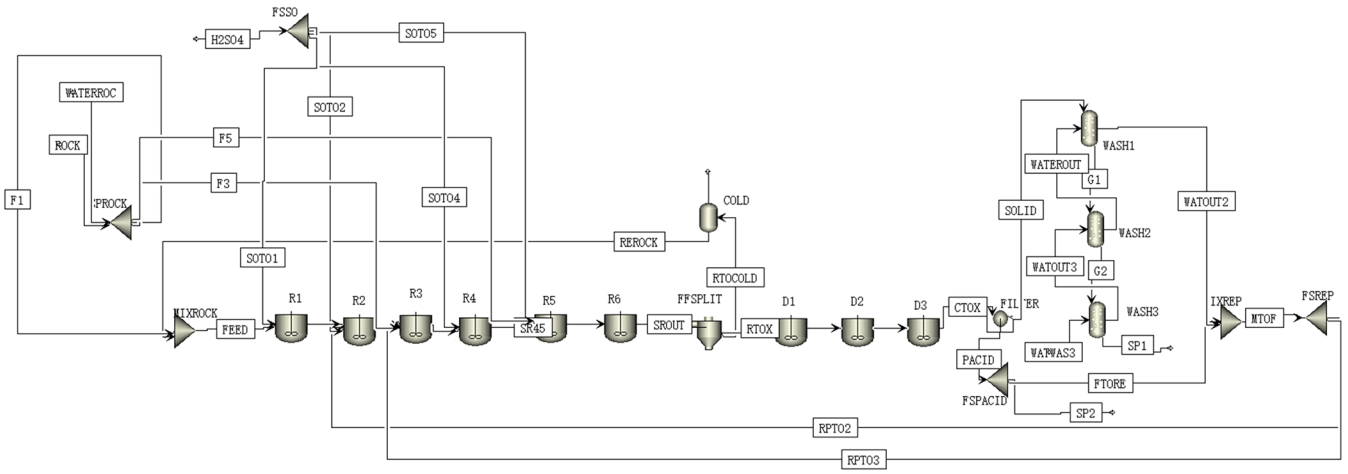

Figure 4. Aspen Plus simulation for WPAP.

energy balance of a real-word factory using Aspen and introduce reaction kinetic models from the literature. Second, we sample data from the established mechanistic model and acquire the required real-world production data from the plant's distributed control system (DCS). Subsequently, we develop a surrogate model using mechanistic data and then perform transfer learning with real-world data to adapt to the real-world production under different optimization scenarios.

https://doi.org/10.1021/acs.iecr.5c03286
Ind. Eng. Chem. Res. 2025, 64, 24138−24155

Finally, the MLSQP algorithm is used for optimization, which can converge to the KKT point of the surrogate model. The detailed procedures are as follows:

3.1. First-Principles Model. In this work, the first-principles model is implemented by Aspen Plus V14, as shown in Figure 4. First, the ELECNRTL method is selected. Second, the reaction tanks and digestion tanks are modeled using RCSTR blocks. Splitter units are simulated with FSplit (for stream splitting based on flow rate) and SSplit (for solid-phase splitting). The flash cooling evaporation process is modeled using a FLASH block. The filter is represented by a FILTER block. The washers are simulated by using SWash blocks. Third, the accuracy of the process model should be improved by tuning some important parameters to minimize model−plant mismatch. For example, in a real-world plant, the material flowing from the reaction tank to the digestion tank is discharged through the overflow outlet and is not a homogeneous liquid−solid mixture. Therefore, a homogeneous splitter cannot be used directly. To simulate this heterogeneous overflow, we employ an SSplit unit to set the split ratios for the solid and liquid phases separately. However, these split ratio parameters cannot be obtained from actual production processes. Thus, we use the bisection method to find the split ratio parameters that achieve model−plant matching with the calculation based on the density of the actual outlet stream. The main parameters include the solid-phase split ratio in the SSplit unit, the recycle acid split ratio, and the washing efficiency. The bisection method is employed to iteratively search for the parameter value that yields model output matching the real-world nominal operating condition. The flowchart is shown in Figure S2 of the Supporting Information.

Besides, among all the units, the thermodynamics and kinetics of the chemical reactions occurring in the reactors are the most critical. They influence the extent of the reaction and ultimately determine phosphorus loss. Therefore, the selection of kinetic models and the inversion of missing parameters are introduced in the following subsections.

3.1.1. Kinetic Model of the Attack of Phosphate Ore. In reactors, the main reactions are the acidolysis of phosphate ore, as shown in Table S3(r1) and (r2) in Supporting Information. The apparent kinetic equation from Soussi-Baatout et al.,[20] as shown in eq 18, is adopted.

$$1 - 3(1 - X)^{2/3} + 2(1 - X) = \left[k\left(\frac{L}{S}\right)^{a} C^{b} D^{c} \mathrm{SS}^{d} \exp\left(\frac{E_a}{RT}\right)\right] \times t \tag{18}$$

Where X is the conversion rate of phosphate ore, (L/S) is the liquid−solid ratio, C is the phosphoric acid concentration (converted as P_2O_5), D is the particle size factors, SS is the stirring speed, T is the temperature, and t is the residence time. k, a, b, c, and d are the fitted parameters. The reaction kinetics are implemented with a user-defined kinetic subroutine in Fortran.

Simultaneously, the side reactions between impurity metal oxides in the ore and the acid were taken into account, and their apparent reaction kinetics are expressed in the following form:[22]

$$1 - 3(1 - X_m)^{2/3} + 2(1 - X_m) = \left[kD^{a} C^{b} P^{c} \exp\left(\frac{E_a}{RT}\right)\right] \times t \tag{19}$$

Where $m \in \{K_2O, M_gO, Al_2O_3\}$, E_a is the activation energy, and P is the P_2O_5-to-CaO ratio.

The side reaction between Fe_2O_3 and acid is governed by surface chemical reactions, and its apparent reaction kinetics are described below:[22]

$$1 - (1 - X_{\mathrm{Fe}})^{1/3} = \left[kD^{a} C^{b} P^{c} \exp\left(\frac{E_a}{RT}\right)\right] \times t \tag{20}$$

3.1.2. Equilibrium Constant Function of Precipitation, Dissolution, and Ion Ionization. Digestion tanks calculate the equilibrium constant with the solubility function for $CaSO_4 \cdot 2H_2O$. The precipitation−dissolution equilibrium constants of gypsum crystals and calcium hydrogen phosphate crystals are calculated using solubility functions, as shown in eq 21, and the data are sourced from Abutayeh and Campbell:[23]

$$\ln K_i = \ln K_i^{\circ} - \frac{\Delta H_i^{\circ}}{R}\left(\frac{1}{T} - \frac{1}{T^{\circ}}\right) - \frac{\Delta Cp_i^{\circ}}{R}\left(\ln\frac{T^{\circ}}{T} - \frac{T^{\circ}}{T} + 1\right) \tag{21}$$

Where K_i is the equilibrium constant, T is temperature, R is the ideal gas constant, ΔH is the mixed enthalpy, and ΔCp is the mixed heat capacity; superscript $^{\circ}$ represents the reference status. In addition to the precipitation−dissolution equilibrium, this model is also used exclusively to describe the ionization of HSO_4^- and the first and second ionizations of H_3PO_4. The model parameters were also determined according to Abutayeh and Campbell.[23]

3.1.3. Kinetics Model for Other Metal Phosphate Crystals. Due to the absence of the kinetic data on metal phosphate crystallization, primarily including (r8), (r11), and (r12) as shown in Table S3 in Supporting Information, production data under nominal operating conditions is used to fit the model. The expression of the power-law kinetic model is as follows:

$$r = k_m c^{n} \tag{22}$$

Where r is the reaction rate, c is the reactant concentration, n is the reaction order, and k_m is the reaction rate constant, governed by the Arrhenius equation:

$$k_m = A \exp\left(-\frac{E_a}{RT}\right) \tag{23}$$

where A is the pre-exponential factor, E_a is the activation energy, R is the ideal gas constant, and T is the absolute temperature. The parameters that need to be estimated are A and E_a. Therefore, the estimation problem of reaction kinetic parameters can be transformed into the following optimization problem:

$$\min_{A^M, E_a^M \in \mathbb{R}} \quad (\mathrm{MF}^{\mathrm{NP}} - 0.505\%)^2 \qquad \text{s.t.} \quad \mathrm{MF}^{\mathrm{NP}} = \mathrm{Aspen}(A^M, E_a^M) \tag{24}$$

Where $\mathrm{MF}^{\mathrm{NP}}$ is the mass fraction of NWSP in phosphogypsum and the superscript M represents metal phosphate. This optimization problem is solved by directly calling the Aspen simulation using the particle swarm

https://doi.org/10.1021/acs.iecr.5c03286
Ind. Eng. Chem. Res. 2025, 64, 24138−24155

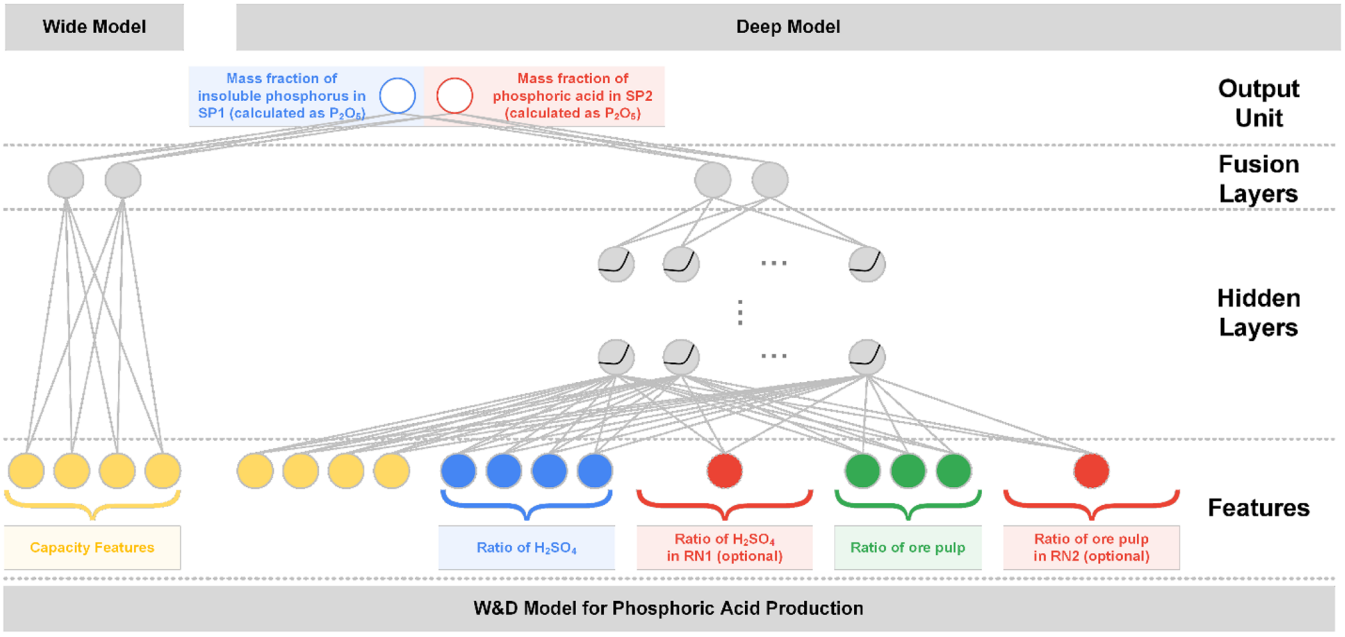

Figure 5. Structure of W&D model.

optimization (PSO) algorithm. The overall procedure is illustrated in Figure S3 of the Supporting Information. First-order kinetics were assumed for all reactions. For (r11) and (r12), the result is $AM = 0.2619$ and $E_a^M = 40.5759$ kJ·mol^{-1}, while for (r8), $A^M = 1.7201$ and $E_a^M = 38.8654$ kJ·mol^{-1}.

3.2. Data Collection and Analysis. Since the simulation parameters of the mechanism model are only based on nominal operating conditions, deviations in model predictions may arise when operating conditions change. Additionally, the presence of multiple recycle streams renders the simulation significantly time-consuming. Thus, this work intends to combine simulation data with real-world industrial data to jointly train a surrogate model for subsequent optimization.

The sampling features mainly include load and branch proportion data. The capacity data specifically covers the total feed flow rate of sulfuric acid, the total feed flow rate of ore pulp, and the flow rate of washing water, while the branch ratio data includes the proportion of feed sulfuric acid entering reaction tanks 1, 2, 4, and 5 (and RN1), as well as the proportion of feed ore pulp entering reaction tanks 1, 3, and 5 (and RN2). The label includes the mass fraction of NWPS in phosphogypsum (converted to P_2O_5) and the mass fraction of phosphoric acid in crude phosphoric acid (converted to P_2O_5).

Industrial production data naturally satisfies the normalization conditions and box constraints (e.g., constraints (4), (5), (7), and (8) in the optimization model). However, when sampling from the mechanistic model, the generated feature data are highly likely to violate these constraints. Therefore, this work develops a hybrid sampling method, illustrated in Sections S8 and S9 of the Supporting Information, to ensure that the sampled feature data meets the aforementioned constraints.

Additionally, we also used the Pearson correlation coefficient to analyze the linear relationships between features and labels, which were applied to determine the structure of the surrogate model. The calculation formula of the Pearson correlation coefficient is shown in eq 25:

$$r = \frac{n\sum_n^{i=1} x_i y_i - \left(\sum_n^{i=1} x_i\right)\left(\sum_n^{i=1} y_i\right)}{\sqrt{\left[n\sum_n^{i=1} x_i^2 - \left(\sum_n^{i=1} x_i\right)^2\right]\left[n\sum_n^{i=1} y_i^2 - \left(\sum_n^{i=1} y_i\right)^2\right]}} \tag{25}$$

where r denotes the Pearson correlation coefficient, n represents the number of samples, x_i is the i-th sample value of the feature (e.g., load features or branch proportion features), and y_i is the corresponding i-th sample value of the label. The results show that the capacity features have relatively significant linear relationships with the label, while the branch proportion features exhibit nonlinear relationships with the label. Further explanations and analyses are provided in the Results section.

3.3. Construction of Surrogate Model. As mentioned above, we need to use simulation and industrial data to jointly train a surrogate model for optimization. In this work, we use the Wide and Deep (W&D) model as a surrogate because it can handle both linear and nonlinear relationships between features and labels. Then, we use transfer learning techniques to fine-tune surrogate models under different scenarios.

3.3.1. Wide and Deep Model. In this work, we apply the Wide and Deep (W&D) model to regression tasks due to the similarity in data characteristics, which was first used for recommender systems.[37] The W&D model for phosphoric acid production is as shown in Figure 5. The output features are the concentration of phosphoric acid in the product and the NWSP content in the phosphogypsum. In the wide part, the model captures several key features: the capacities of sulfuric acid, phosphate ore, water in pulp, and washing water, all of which exhibit an approximately linear correlation with the outputs. In the deep part, a more comprehensive set of features is considered, including both capacity-related variables and ratio-based features, to account for their complex nonlinear relationships with the system responses.

3.3.2. Training W&D Model. First, we train the W&D model with both simulation data and production data, as shown in Figure 6(a). The simulation data used are under

https://doi.org/10.1021/acs.iecr.5c03286
Ind. Eng. Chem. Res. 2025, 64, 24138−24155

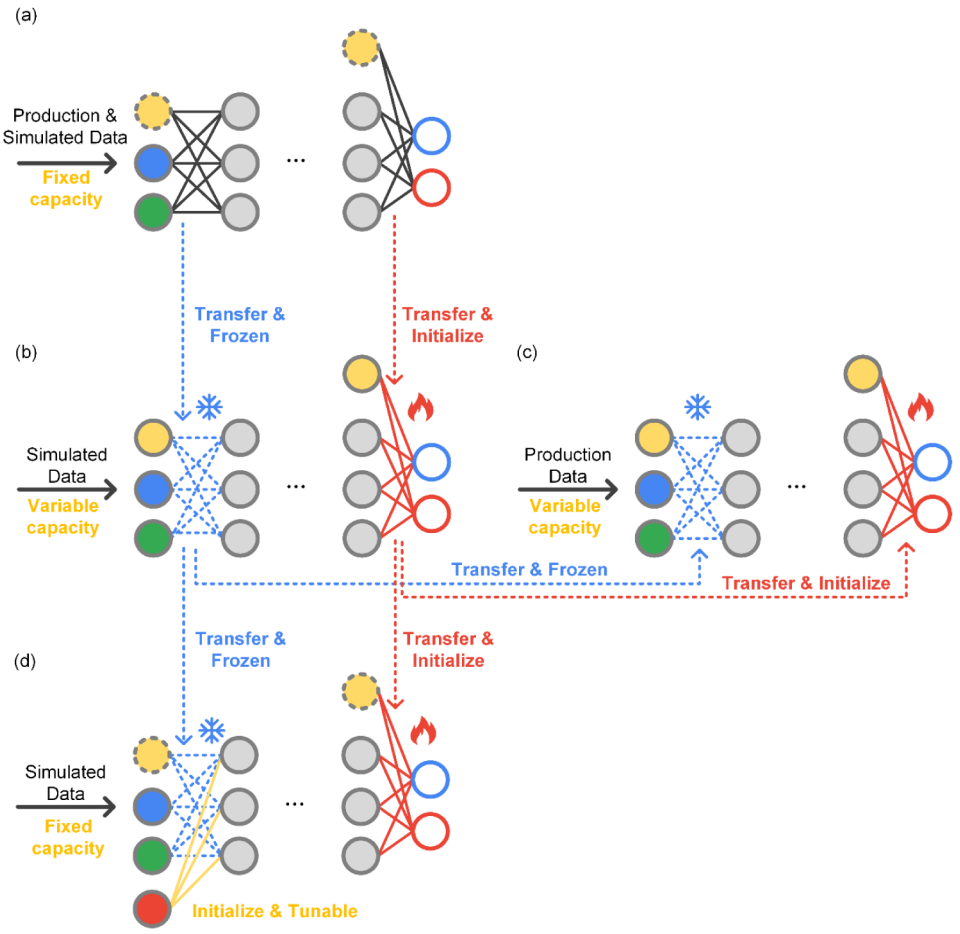

Figure 6. Schematic diagram of the relationship among surrogates and the corresponding transfer learning method.

Table 1. Summary of Surrogate Models' Information

No.	Name	Train	Valid	Test	Simulated data	Prodaction data	Loss function	Optimization scenario
(a)	Foundation	10 162	1412	1412	√	√	WMES	1
(b)	Load (simulation data)	10 000	1250	1250	√	-	MES	-
(c)	Load (real-world data)	500	69	69	-	√	CL	2
(d)	New reactor	10 000	1250	1250	√	-	MES	3

constant load (sulfuric acid: 85 m^3/h, ore pulp: 168 m^3/h), which includes 10 000 samples for the training set, 1250 for the validation set, and 1250 for the test set. From the DCS data of the past 6 months, we selected sample points with the same load that simultaneously contained NWSP and phosphoric acid concentration (162 samples in total). However, due to the extremely small amount of production data, we adopt weighted mean-square error (WMSE) as the loss function, as shown in eq 26:

$$\text{Loss} = \frac{N_{\text{dcs}} \sum_{i\in\text{SIM}} (z_i - \hat{z}_i)^2}{N_{\text{sim}}(N_{\text{dcs}} + N_{\text{sim}})} + \frac{N_{\text{sim}} \sum_{j\in\text{DCS}} \text{CL}_j}{N_{\text{dcs}}(N_{\text{dcs}} + N_{\text{sim}})} \tag{26}$$

where SIM is the data set of simulated samples and DCS is the real-world data set; N_{sim} is the number of simulated data and N_{dcs} is the number of real-world data; z is the label of the surrogate model, and $\hat{z}$ is the predicted value of the model. Model (a) is used as the surrogate model of optimization scenario 1 and is named as the Foundation model.

For scenario 2, we require the surrogate model to be capable of predicting the NWSP and phosphate concentration under different loads and branch ratios. The used simulation data and production data are under different loads and branch ratios. The production data include 569 samples in total. We then perform transfer learning on model (a). First, we froze all parameters except those in the wide part and the last two layers of the deep part and trained the model using simulation data, as shown in Figure 6(b). Then, we performed transfer learning on model (b). However, since NWSP data are sampled every 4 h while phosphate concentration data is sampled every 12 h, many samples lack phosphate concentration data. In real-world production, phosphoric acid concentration is controlled within the range of 24−26%, although precise values are lacking , a customer loss (CL) is proposed:

$$\text{CL} = (z_{\text{np}} - \hat{z}_{\text{np}})^2 + \max(0,\ \hat{z}_{\text{pa}} - 26)^2 + \max(0,\ 24 - \hat{z}_{\text{pa}})^2 \tag{27}$$

https://doi.org/10.1021/acs.iecr.5c03286
Ind. Eng. Chem. Res. 2025, 64, 24138−24155

where the subscript np represents the content of NWSP and the subscript pa represents the concentration of phosphoric acid.

For scenario 3, since there is no corresponding real-world system, we only use simulation data under fixed capacity for training. Transfer learning is also employed, as shown in Figure 6(d). Nevertheless, the model structure has been adjusted with the addition of two new features (the branch ratio of RN1 and RN2). Thus, we transferred the parameters corresponding to the structure matching the original model, while directly initializing the parameters for the newly added structure.

The names of the models, the data sets used, and the loss functions employed are presented in Table 1.

3.4. Optimization Algorithm. In this work, the deterministic algorithm MLSQP[38] is employed, as shown in Figure 7. A common approach to incorporating surrogate models into deterministic optimization frameworks is to embed them using a full-space formulation as constraints. However, this typically requires updating a large number of intermediate variables at each iteration, which can be computationally intensive and cumbersome. In contrast, in the proposed MLSQP algorithm, at each iteration, the decision variables are first fed into the surrogate model for prediction. Then, the derivatives of the model outputs with respect to the inputs are computed directly based on this prediction. The proposed algorithm can converge to the KKT point of the surrogate model.

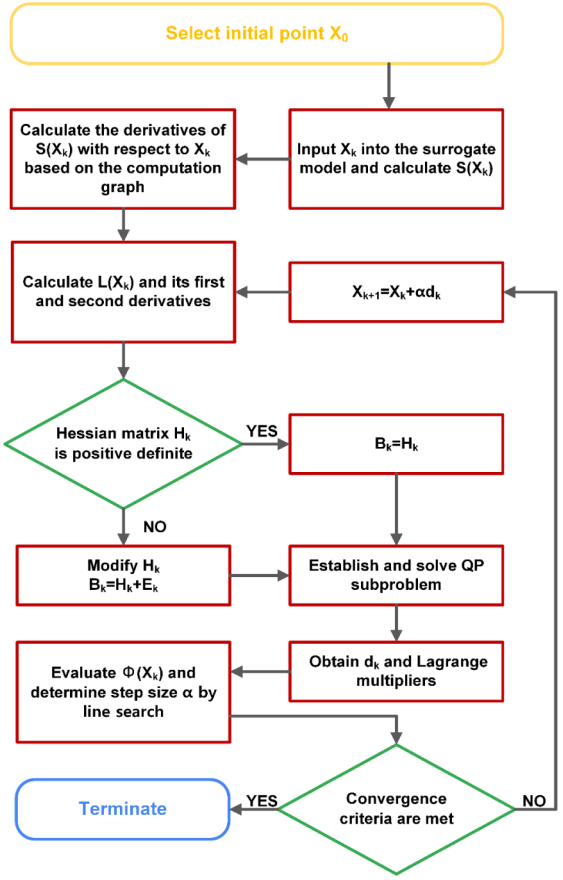

Figure 7. Flowchart of the MLSQP algorithm.

Specifically, this algorithm is built based on the feasible path Sequential Quadratic Programming (SQP) algorithm,[39,40] as shown in Figure 7. First, a set of decision variables (X) is given, which is input into the surrogate model to compute the output S(X), constraints (g and h), objective function (f), and Lagrangian function (L). Based on the computation graph, the derivative of the surrogate model's output S(X) with respect to X is obtained, thereby calculating the gradient of the Lagrangian function with respect to X and the Hessian matrix (H). If H is nonpositive definite, a minimum norm correction is applied to it. A QP subproblem is then constructed using H, and iteration direction (d) is obtained by solving this subproblem. Line search is used to determine the step size α. Subsequently, X is updated until the convergence condition is met.

4. RESULTS

4.1. First-Principles Model Simulation Result. Table 2 shows the simulation results and the relative errors compared with the real-world factory operation data in the steady-state scenario.

Table 2. Comparison between Simulation Results for Key Parameters and Real-World Factory

Nomenclature	Description	Real value	Simulated value	Relative error
M_{SP2}, ton·h^{-1}	Mass flow of SP2	227.00	233.39	2.81%
MF^{P}_{SP2}, %	Mass fraction of P_2O_5 in SP2	25.00	24.89	0.44%
M_{S2}, ton·h^{-1}	Mass flow of S2	391.00	386.00	1.28%
MF^{P}_{S2}, %	Mass fraction of P_2O_5 in S2	16.00−18.00	17.32	0.00%
M_{S1}, ton·h^{-1}	Mass flow of S1	802.00	797.00	0.62%
MF^{P}_{S1}, %	Mass fraction of P_2O_5 in S1	29.00−33.00	33.00	0.00%
M_{SP1}, ton·h^{-1}	Mass flow of SP1	370.00	372.34	0.63%
MF^{L}_{SP1}, %	Mass fraction of liquids in SP1	24.00−26.00	24.24	0.00%
MF^{NP}_{SP1}, %	Mass fraction of nonsoluble phosphorus (characterize with P_2O_5) in SP1	0.505	0.505	0.00%

The yield of phosphoric acid is determined by the flow rate and the concentration of P_2O_5; therefore, we mainly focus on verifying the mass fraction of P_2O_5 and the flow rate of the streams in each unit under the nominal operating condition. Specifically, the relative errors for the mass flow of phosphogypsum (SP1), dilute phosphoric acid (SP2), the stream from the scrubber back to reactor tanks (S1), and the stream from the digestion tank to the filter (S2) are all below 3%; the relative errors for the mass fraction of P_2O_5 in S1, S2, and SP2 are all below 0.5%; the relative errors for the mass fraction of nonsoluble phosphorus (characterized with P_2O_5) in SP1 are 0.00%. However, since parts of the kinetic parameters are fitted based on nominal operating conditions, significant deviations occur at points far from the nominal. For instance, when the load drops to half of the nominal load, the relative error is approximately 66.67%. Therefore, it is necessary to establish a surrogate model by incorporating actual production data.

4.2. Feature Analysis Result. In this work, we use the absolute Pearson correlation coefficient (APCC) to analyze the correlation between features and labels. The result is shown in

https://doi.org/10.1021/acs.iecr.5c03286
Ind. Eng. Chem. Res. 2025, 64, 24138−24155

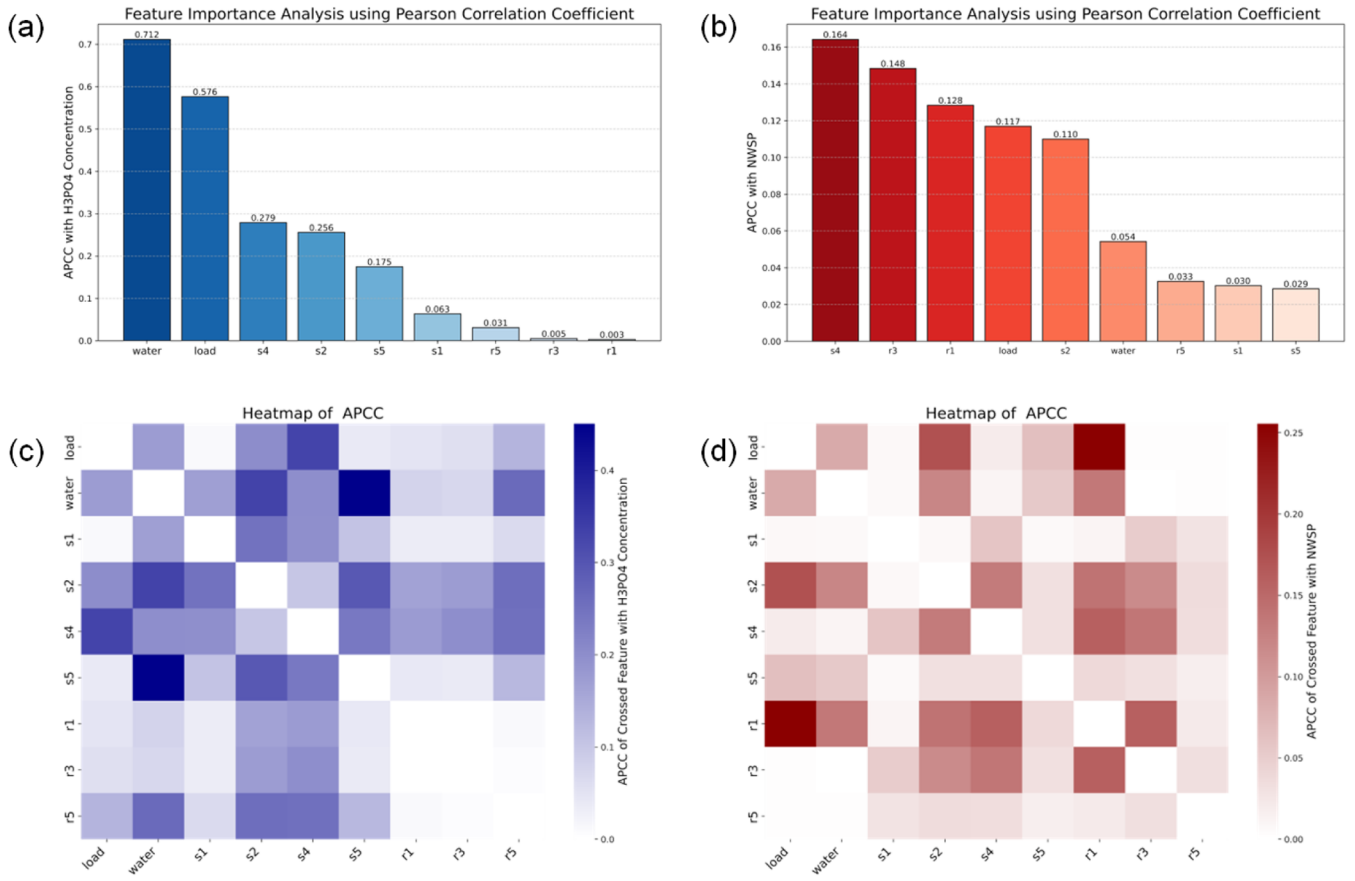

Figure 8. Feature analysis with absolute Pearson correlation coefficient, including (a) features related to H_3PO_4 concentration, (b) features related to NWSP content, (c) crossed features related to H_3PO_4 concentration, and (d) crossed features related to NWSP content.

Table 3. Performance of Different Surrogate Models on Test Data Sets

Model	Indicator	Foundation model		Load model (simulated data)		Load model (real-world data)	New reactor model	
		NSWP	PAC	NSWP	PAC	NSWP	NSWP	PAC
W&D	MSE	5.49×10^{-5}	7.27×10^{-3}	3.23×10^{-4}	2.69×10^{-2}	2.02×10^{-4}	1.63×10^{-5}	1.33×10^{-2}
	R	1.00	1.00	0.99	0.99	1.00	1.00	0.97
	Relative error, %	0.53	0.12	2.19	0.48	0.58	0.47	0.29
SVR	MSE	1.42×10^{-4}	3.35×10^{-2}	3.28×10^{-4}	5.95×10^{-2}	7.07×10^{-2}	7.42×10^{-4}	0.19
	R	0.99	1.00	0.99	0.99	0.66	0.96	0.98
	Relative error, %	1.47	0.35	2.44	0.55	62.62	7.18	1.00
RF	MSE	1.29×10^{-4}	2.72×10^{-2}	3.00×10^{-4}	5.63×10^{-2}	7.02×10^{-2}	9.32×10^{-5}	4.47×10^{-2}
	R	0.99	1.00	0.99	0.99	0.77	1.00	0.99
	Relative error, %	1.24	0.21	2.18	0.53	62.36	1.75	0.40
W&D (without TL)	MSE	-	-	1.55×10^{-3}	0.14	1.82×10^{-3}	1.82×10^{-5}	1.46×10^{-2}
	R	-	-	0.93	0.95	0.92	1.00	0.97
	Relative error, %	-	-	5.73	1.24	7.60	0.72	0.31

Figure 8, where the branching ratios of sulfuric acid are represented by s1, s2, s4, s5, and ore pulp are represented by r1, r3, r5.

For the H_3PO_4 concentration, washing water and production load exhibit strong linear correlations, mainly due to their impact on the system's water balance. Acid distribution ratios show moderate linear correlations, as they influence acid concentration in individual reactors and, consequently, phosphate rock dissolution. For the NWPS content, features s4, r3, r1, load, and s2 show some linear correlation. However, APCC values are generally low, suggesting that linear relationships are insufficient to fully capture feature-label dependencies. Notably, APCC increases when crossed features are considered, indicating that NWPS is better characterized by nonlinear relationships. Therefore, the capacity features, including load and water, are input into the wide part of the W&D model, while all features are input into the deep part.

https://doi.org/10.1021/acs.iecr.5c03286
Ind. Eng. Chem. Res. 2025, 64, 24138−24155

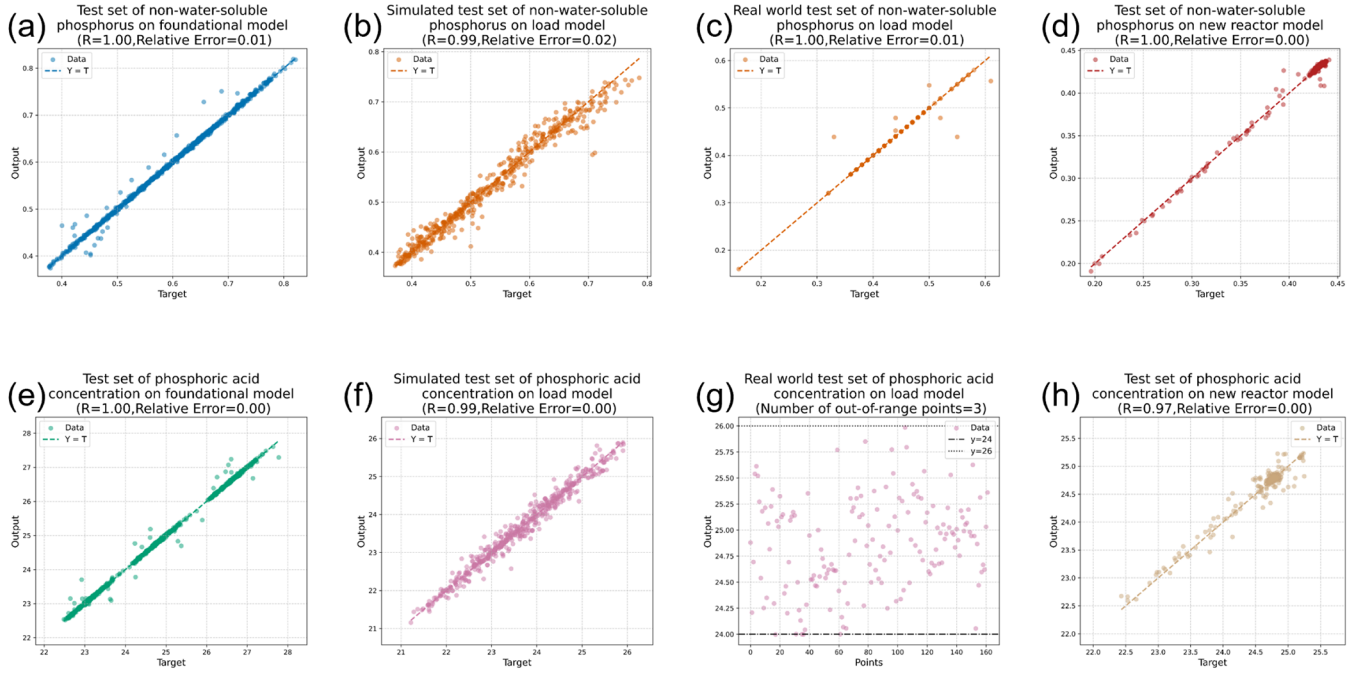

Figure 9. Parity plots over the test set with Pearson correlation coefficient (R) and relative error to evaluate the accuracy of NWSP on (a) foundational model, (b) load model (simulated test set), (c) load model (real word test set), (d) new reactor model, and the phosphoric acid concentration on (e) foundational model, (f) load model (simulated test set), (g) load model (real-world test set), and (h) new reactor model.

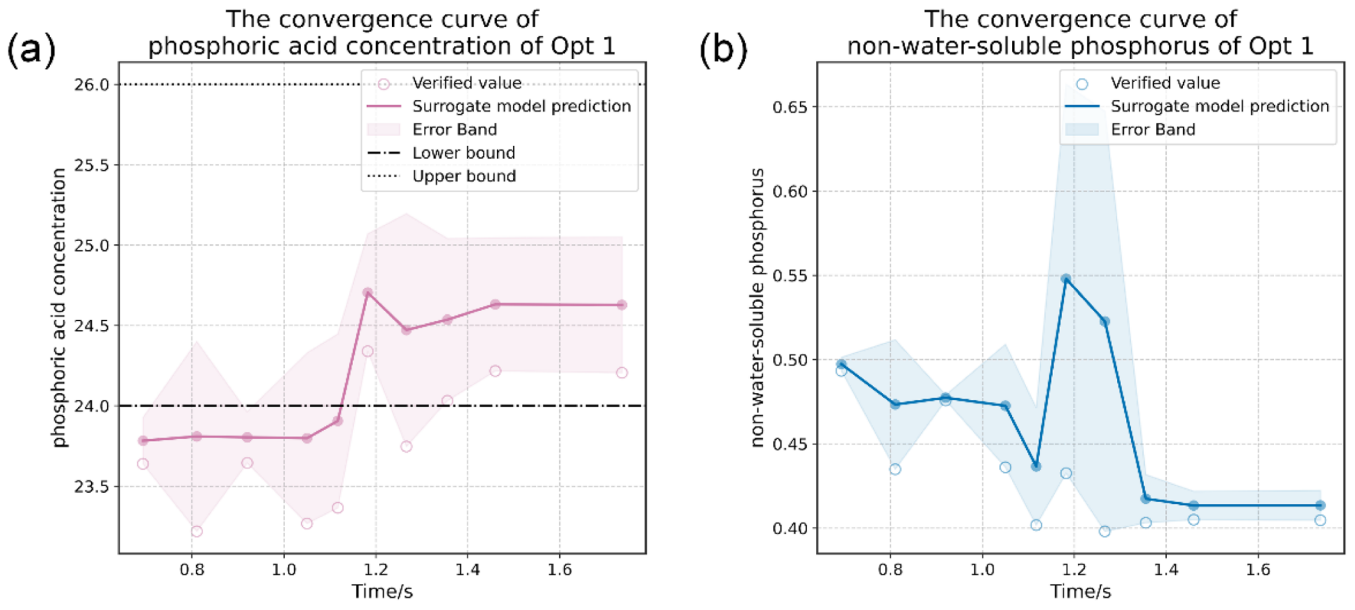

Figure 10. Convergence curve of (a) H_3PO_4 concentration and (b) NWSP under scenario 1.

4.3. Surrogate Model Prediction Result. All surrogate models adopt the W&D model. The middle layers of the Deep part share the same structure, which is organized as input—512-dimensional layer (×3)—256-dimensional layer (×3)—128-dimensional layer (×3)—64-dimensional layer (×2)—32-dimensional layer (×2)—16-dimensional layer (×2)—output. The activation function for the Deep part is selected as the Swish function. All surrogates are trained with the Adam optimizer.

For the Foundation model, batch size is set to 64, the learning rate is set to 0.001, and the number of epochs is set to 2000. For the Load model (simulation data) and the new reactor model, batch size is set to 64, the learning rate is set to 0.0005, and the number of epochs is set to 1000. For the Load model (production data), batch size is set to 16, learning rate is set to 0.0001, and the number of epochs is set to 500.

A high-precision surrogate model is the cornerstone for ensuring the reliability and practicality of optimization results. The performance of the W&D models established for 3 optimization scenarios on the test set is shown in Table 3 and Figure 9. Specifically, for simulated data sets shown in Figure 9(a, b, d–f, h), all 3 models show the capacity to accurately predict, with the worst-case scenario where the Pearson correlation coefficient is 0.97 and the average relative error is

https://doi.org/10.1021/acs.iecr.5c03286
Ind. Eng. Chem. Res. 2025, 64, 24138−24155

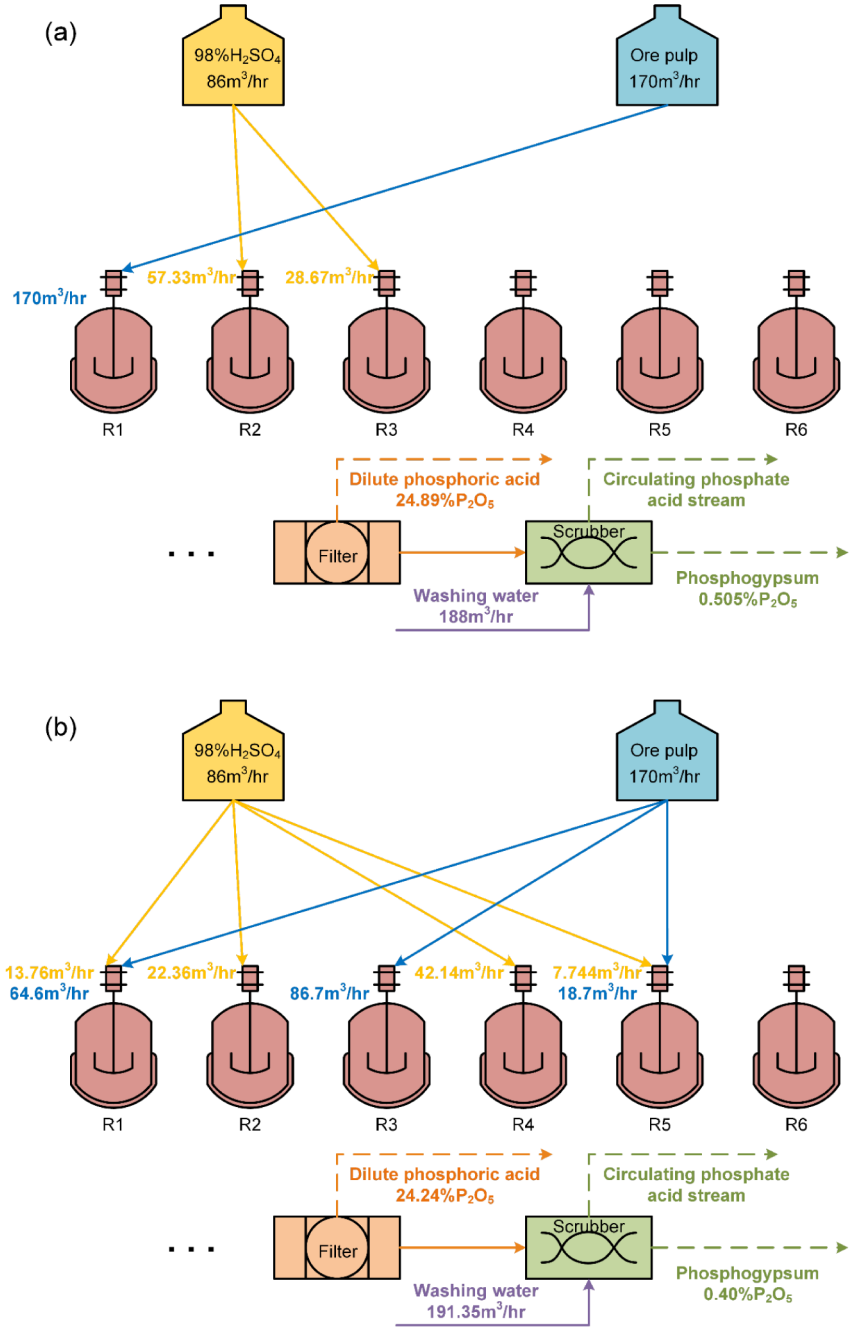

Figure 11. Comparison between results (a) before optimization and (b) after optimization under scenario 1.

0.02%. For a real-world data set, the prediction of NWSP is precise, and the accuracy of phosphoric acid concentration falling within the correct range [24%, 26%] is 98.8%. To further demonstrate the accuracy of our proposed surrogate model, we also compare it with support vector regressor (SVR) and random forest (RF), both of which have undergone hyperparameter tuning. The accuracy of predicting NWSP and phosphoric acid concentration (PAC) for the 3 models is shown in Table 3.

The W&D model outperforms SVR and RF on the test sets for both the baseline and new reactor tasks. For the load task, while the W&D model's accuracy for the NSWP feature in simulated data is marginally lower than that of the other models, the performance of SVR and RF on real-world data sets is notably poor. Given these results, it is reasonable to conclude that the W&D model achieves higher accuracy than traditional machine learning models across all 3 tasks. On the other hand, when the W&D model is trained with the same hyperparameters but without transfer learning, its performance is notably inferior compared to when it is trained using transfer learning. This highlights the significant benefit that transfer learning (TL) brings to the optimization and accuracy of the W&D model in the context of WPAP.

4.4. Optimization Result. All optimization problems are solely solved on a laptop with an AMD Ryzen 7 7840H processor and Radeon 780M Graphics (3.80 GHz). The initial point of MLSQP is set at the point with the minimal NWSP in the data set, with the maximum number of total iterations set to 500 and the maximum iterations for line searches set to 20. For PSO applied to surrogate-based optimization, the

https://doi.org/10.1021/acs.iecr.5c03286
Ind. Eng. Chem. Res. 2025, 64, 24138−24155

Table 4. Comparison with the Commonly Used Framework under Scenario 1

Method	Load	NWSP, %	PAC, %	Optimization time/s	Status
PSO-surrogate	1	0.41	24.94	27.86	Success
PSO-rigorous	1	0.43	24.43	-	Success
SQP (Aspen)	1	-	-	-	Opt Fail
MLSQP-surrogate	1	0.41	24.51	1.73	Success

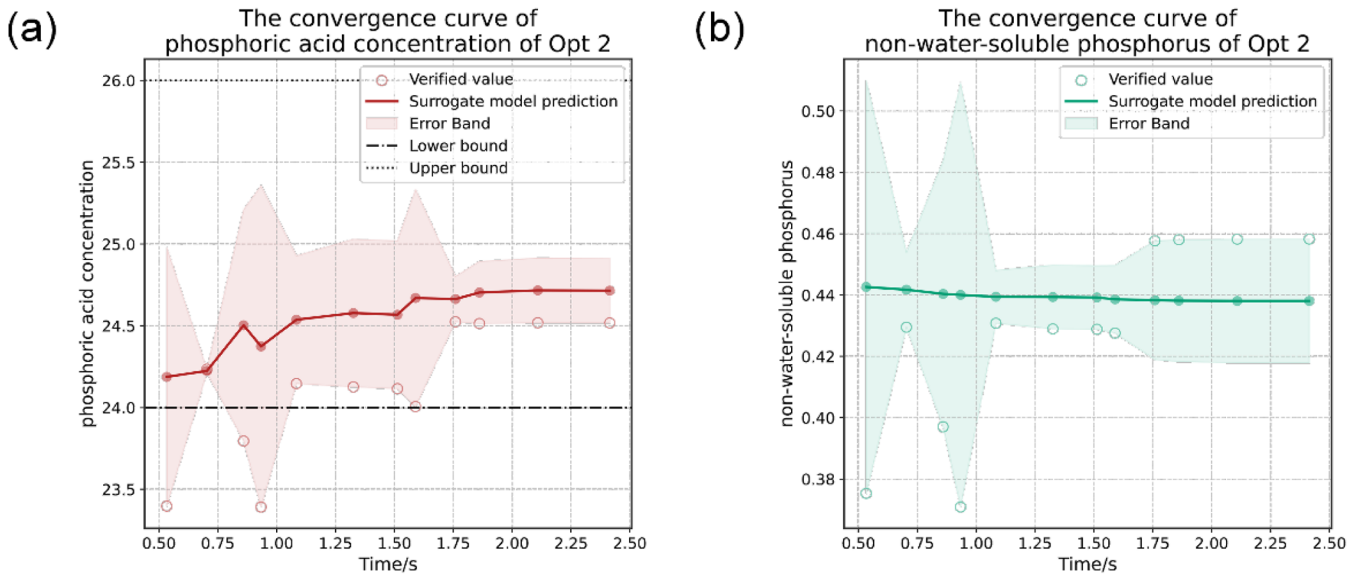

Figure 12. Convergence curve of (a) H_3PO_4 concentration and (b) NWSP under scenario 2.

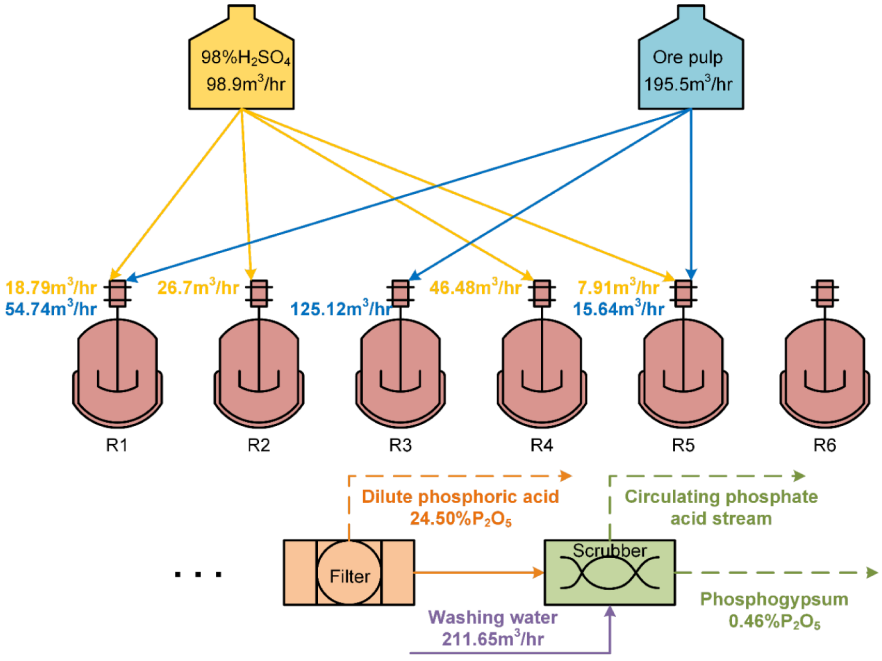

Figure 13. Optimization result under scenario 2.

population size is set to 100, and the number of iterations is set to 100. For the PSO applied to rigorous model-based optimization, the population size is set to 50, while the number of iterations remains at 100.

4.4.1. Optimization Scenario 1. The convergence curve of H_3PO_4 concentration and NWSP content of scenario 1 is shown in Figure 10, where solid circles represent the predictions of the surrogate model, while hollow circles denote the values validated in the rigorous model. The primary solution, as well as the validated solution, has been rigorously checked and is found to fully comply with all predefined constraints. This ensures that the results meet the necessary standards and requirements. The optimization problem is solved in 1.7 s, and the content of NWSP in scenario 1 is reduced by 20.79% compared to the current operating conditions as shown in Figure 11(a).

https://doi.org/10.1021/acs.iecr.5c03286
Ind. Eng. Chem. Res. 2025, 64, 24138−24155

Table 5. Comparison with the Commonly Used Framework under Scenario 2

Method	Load	NWSP, %	PAC, %	Optimization time/s	Status
PSO-surrogate	1.15	0.44	24.10	48.68	Success
PSO-rigorous	1.12	0.39	24.88	-	Success
SQP (Aspen)	-	-	-	-	Opt Fail
MLSQP-surrogate	1.15	0.44	24.54	2.41	Success

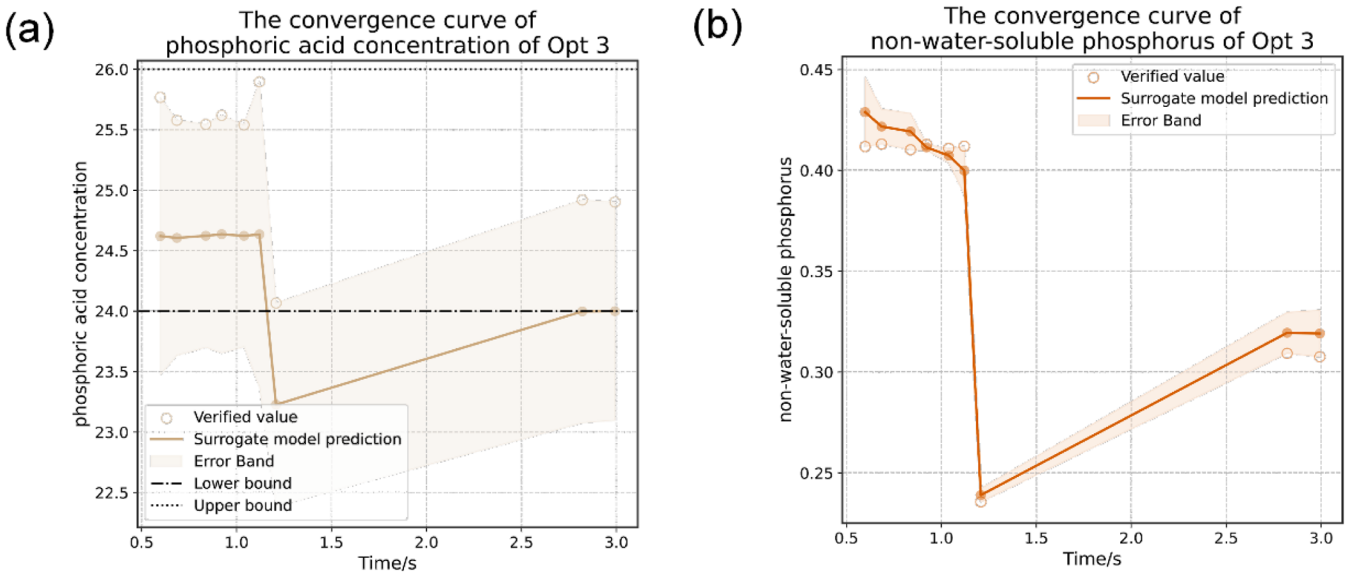

Figure 14. Convergence curve of (a) H_3PO_4 concentration and (b) NWSP under scenario 3.

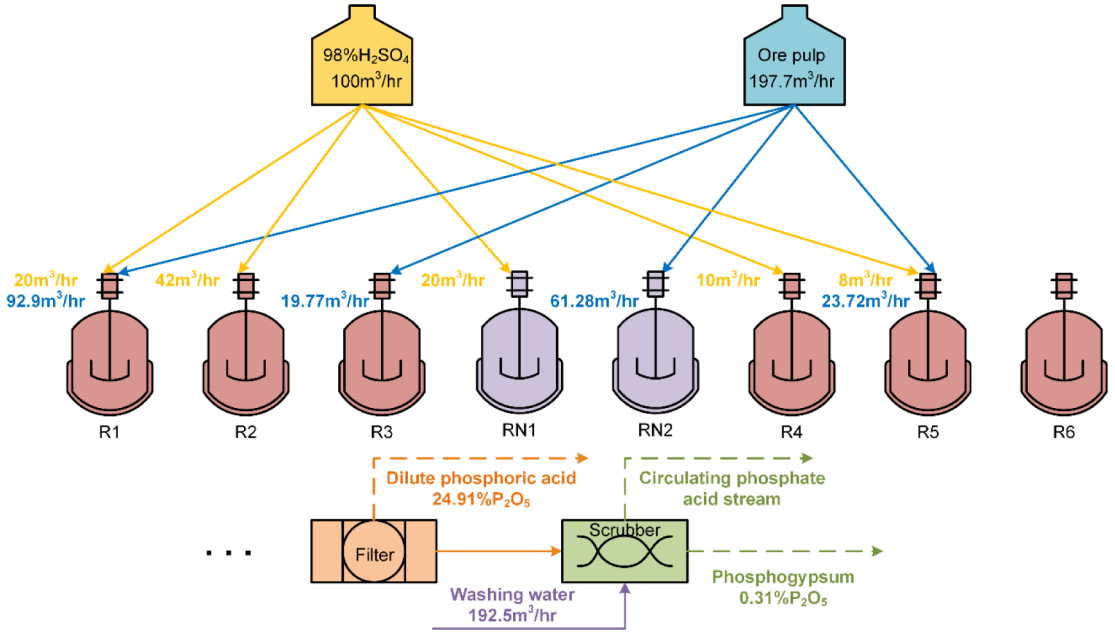

Figure 15. Optimization result under scenario 3.

The distribution of H_2SO_4 and ore pulp, as well as the load of washing water, is shown in Figure 11(b), and the H_3PO_4 concentration and NWSP content (validated in a rigorous model) are also provided. The distribution of H_2SO_4 and ore pulp into distinct reactors has been shown to markedly decrease the content of NWSP in phosphogypsum. This effect is primarily due to the maintenance of suitable SO_3 and P_2O_5 concentrations in each reactor, which facilitates maximal acid dissolution while simultaneously reducing the precipitation of dicalcium phosphate dihydrate (DCPD) crystals.

To further validate the effectiveness of the proposed framework, we conducted comparative experiments with several existing approaches. These include the SQP optimizer built into Aspen, optimization using PSO to directly call the rigorous model, which requires thousands of simulations and takes several days to complete, and optimization using PSO with a surrogate model. The number of PSO's evaluations to

https://doi.org/10.1021/acs.iecr.5c03286
Ind. Eng. Chem. Res. 2025, 64, 24138−24155

Table 6. Comparison with Commonly Used Framework under Scenario 3

Method	Load	NWSP, %	PAC, %	Optimization time/s	Status
PSO-surrogate	1.16	0.32	24.00	28.19	Success
PSO-rigorous	1.16	0.39	24.30	-	Sim Fail
SQP (Aspen)	1.16	-	-	-	Opt Fail
MLSQP-surrogate	1.16	0.32	24.00	2.99	Success

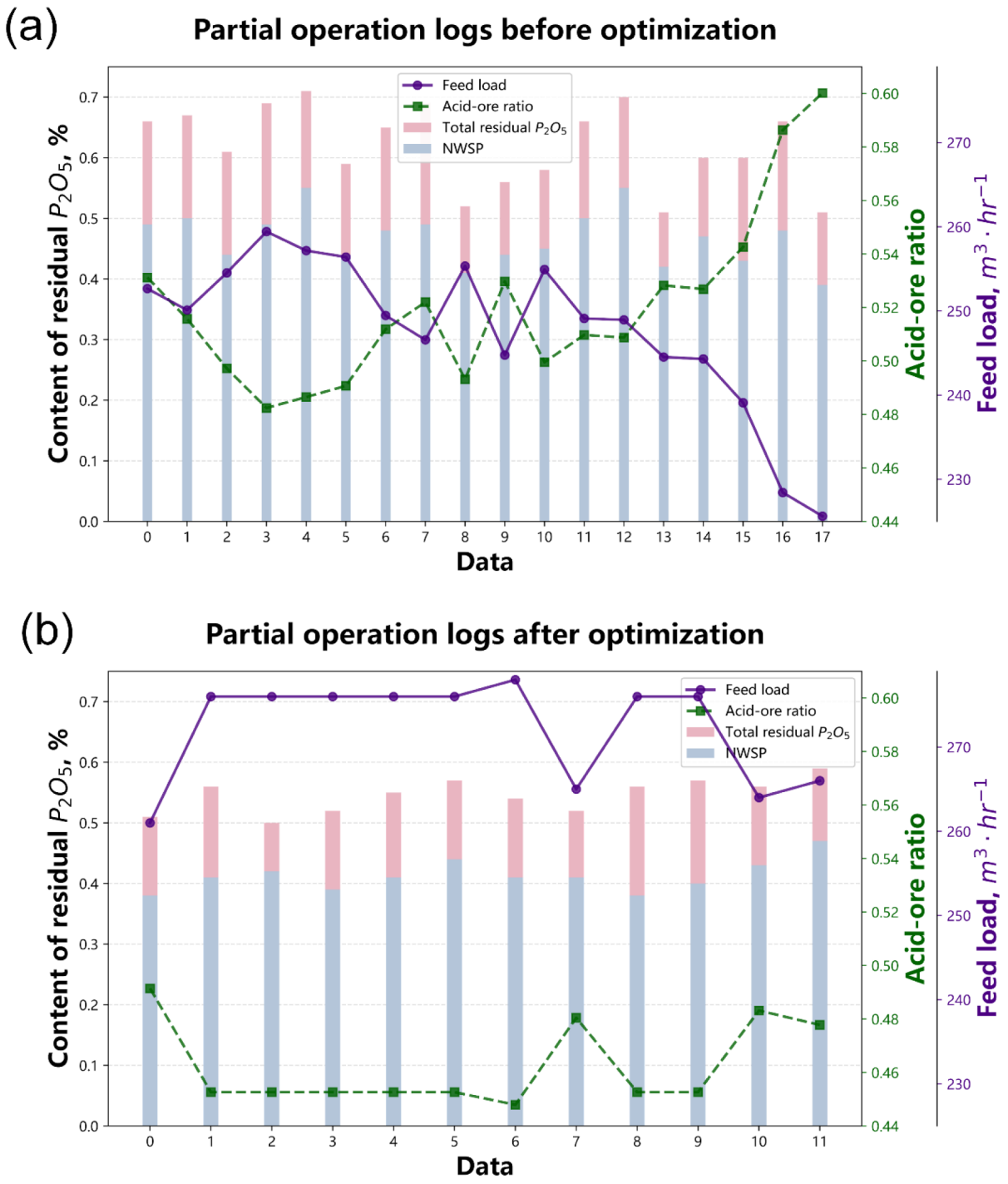

Figure 16. Partial operation logs and corresponding content of residual phosphorus (a) before and (b) after using optimized results in the real-world factory.

the rigorous model (iteration number times population size) is set to be equal to the sampling number used for constructing the surrogate model. To ensure that the input variables generated by PSO satisfy the constraints, a feasibility rule was designed to reduce the probability of generating infeasible solutions. The results are listed in Table 4. The attempt to

https://doi.org/10.1021/acs.iecr.5c03286
Ind. Eng. Chem. Res. 2025, 64, 24138−24155

Table 7. Comparison of the Average Values of Indicators before and after Implementing the Optimization Result

				Gypsum		
Index	Sulfuric acid load, $m^3 \cdot h^{-1}$	Ore pulp load, $m^3 \cdot h^{-1}$	Acid-to-ore ratio	Total phosphorus, %	Water-soluble phosphorus, %	NWSP, %
Before optimization	83.85	165.39	0.51	0.60	0.15	0.45
After optimization	84.27	181.50	0.46	0.55	0.14	0.41

solve the problem using Aspen's built-in SQP solver failed to converge. All PSO and MLSQP methods succeeded, and the optimization results can be successfully simulated in the rigorous model. PSO-rigorous provides an optimized result but not the optimal one. Although PSO-surrogate and MLSQP-surrogate lead to close solutions, which are better than PSO-rigorous, MLSQP has a significant advantage in time consumption and can ensure convergence to the KKT point of the surrogate model compared to PSO-surrogate.

4.4.2. Optimization Scenario 2. The convergence curve of H_3PO_4 concentration and NWSP content of scenario 2 is shown in Figure 12. The optimization problem is solved in 2.3 s. The content of NWSP in scenario 2 is reduced by 8.91%, and the production load is increased by 15% compared to the current operating conditions, as shown in Figure 11(a). Note that the optimal objective consists of load multiplier (1.15) and the content of NWSP, which equals 0.44% in the primary result and 0.46% in the verified result. According to the verification, the optimization results meet the constraints. The optimization result is shown in Figure 13. As previously analyzed, when the H_2SO_4 and ore pulp are concentrated in R3 and R4 (the middle section of the reaction system), the NWSP is relatively low, despite the production load being increased.

The comparison with other commonly used frameworks under scenario 2 is as shown in Table 5. The attempt to solve the problem using Aspen's built-in SQP solver still failed to converge. All PSO and MLSQP succeeded. However, MLSQP shows the best performance among these frameworks, both in time consumption and solution.

4.4.3. Optimization Scenario 3. The convergence curve of H_3PO_4 concentration and NWSP content in scenario 3 is shown in Figure 14. The optimization problem is solved in 3.0 s. The content of NWSP in scenario 3 is reduced by 38.61% compared to the current operating conditions shown in Figure 11(a). According to the verification, the optimization results meet the constraints. The optimization result is shown in Figure 15. The addition of two extra reactors, along with a recirculation system, leads to a more uniform distribution of phosphoric acid and ore pulp during the process, resulting in a lower NWSP content.

The attempt to solve the problem using Aspen's built-in SQP solver still failed to converge. According to Table 6, PSO-rigorous was successfully solved but resulted in a suboptimal solution, and the corresponding solution failed to converge during simulation-based validation in Aspen. The results obtained using MLSQP and PSO with the surrogate model were generally consistent; however, MLSQP demonstrated significantly faster computation speed compared to PSO.

4.5. Real-World Validation. Optimization models are typically constructed based on a series of assumptions and ideal conditions, which may not always be fully applicable in real-world scenarios. By validating the solution within actual factory environments, it can be ensured that the optimization strategies are both practical and effective, thereby bridging the gap between theoretical expectations and practical outcomes.

The optimized result of scenario 1 is validated in a real-world factory, and the operation logs and the corresponding content of residual phosphorus are as shown in Figure 16. As the total load increases, the residence time of the material decreases. To maintain a low level of NWSP content, it is necessary to increase the acid-to-ore ratio in order to enhance the reaction rate. While this adjustment effectively improves process efficiency, it also leads to higher consumption of sulfuric acid. Contrary to expectations, the implementation of our optimization result showed that it could achieve lower residual phosphorus levels even when handling larger material loads by tuning the feed ratio between different tanks. Remarkably, this was accomplished while simultaneously using smaller acid-to-ore ratios.

The comparison of the average values of key indicators before and after implementing the optimization results is shown in Table 7. With a 6.6% increase in total load and a 9.8% reduction in the acid-to-ore ratio, our optimization result achieved an 8.3% reduction in total residual phosphorus and an 8.9% reduction in NWSP, all without any additional energy or raw material consumption. This outcome highlights the efficiency and effectiveness of our optimized process, demonstrating its capability to enhance performance under more demanding conditions while maintaining resource efficiency.

5. CONCLUSION

In this work, we employ surrogate-assisted optimization to help alleviate the issues of low phosphorus recovery and phosphogypsum pollution in wet-processed phosphoric acid production. Specifically, we first addressed the absence of an accurate mechanistic model. Although numerous studies have been devoted to developing kinetic models for wet-process phosphoric acid production, effective integration with the process simulation has remained elusive. By leveraging both the literature and real-world production data, we selected an appropriate model for the actual industrial process and performed parameter inversion to identify the missing kinetic parameters, thereby bridging this research gap.

Although mechanistic models can accurately capture production trends and provide a uniform sample distribution, a first-principles model cannot maintain high accuracy in all working conditions. Besides, their simulations often suffer from slow convergence and frequent divergence due to the nested multilevel recycle streams. To enhance the robustness of the optimization framework and ensure reliable performance, we introduce a surrogate model for optimization purposes. The structure and features of the surrogate model are carefully designed based on feature importance evaluation. The MLSQP algorithm is introduced to solve optimization problems under 3 different scenarios, ensuring convergence to the KKT point of the surrogate model. Compared with PSO, it also demonstrates lower computational time consumption.

The optimizations under 3 scenarios achieved reductions of 20.79%, 8.91%, and 38.61% in NWSP, respectively, compared to nominal operating conditions. The real-world tests

https://doi.org/10.1021/acs.iecr.5c03286
Ind. Eng. Chem. Res. 2025, 64, 24138−24155

confirmed an 8.3% reduction in total residual phosphorus and an 8.9% decrease in NWSP, without increasing energy or raw material consumption. The satisfactory optimization results demonstrate that the optimization of the wet-process phosphoric acid production is successful and show its potential for application in optimizing similar chemical processes.

■ ASSOCIATED CONTENT

Supporting Information

The Supporting Information is available free of charge at https://pubs.acs.org/doi/10.1021/acs.iecr.5c03286.

Additional data, methods, and algorithms for simulation and sampling (PDF)

■ AUTHOR INFORMATION

Corresponding Authors

Xin Xiao − *Institute of Process Engineering, Chinese Academy of Science, Beijing 100190, China; Work Committee on Carbon Neutral Intelligent Industry Innovation, China Institute for Innovation and Development Strategy, Beijing 100044, China*; Email: xxiao@ipe.ac.cn

Yujiao Zeng − *Institute of Process Engineering, Chinese Academy of Science, Beijing 100190, China*; Email: yjzeng@ipe.ac.cn

Authors

Zixuan Zhang − *Institute of Process Engineering, Chinese Academy of Science, Beijing 100190, China; School of Chemical Engineering, University of Chinese Academy of Science, Beijing 100049, China*; orcid.org/0009-0006-7354-0499

Xiaowei Song − *Institute of Process Engineering, Chinese Academy of Science, Beijing 100190, China; School of Chemical Engineering, University of Chinese Academy of Science, Beijing 100049, China*

Jianhua Chen − *Institute of Process Engineering, Chinese Academy of Science, Beijing 100190, China*; orcid.org/0000-0002-4068-3956

Limin Wang − *Institute of Process Engineering, Chinese Academy of Science, Beijing 100190, China; School of Chemical Engineering, University of Chinese Academy of Science, Beijing 100049, China*; orcid.org/0000-0003-2543-3622

Songlin Liu − *State Key Laboratory of Green and Efficient Development of Phosphorus Resources, Guiyang 550081, China*

Shaoxiu Xue − *State Key Laboratory of Green and Efficient Development of Phosphorus Resources, Guiyang 550081, China*

Zhiwu Zhou − *State Key Laboratory of Green and Efficient Development of Phosphorus Resources, Guiyang 550081, China*

Jie Li − *Centre for Process Integration, Department of Chemical Engineering, School of Engineering, The University of Manchester, Manchester M13 9pl, U. K.*; orcid.org/0000-0001-5196-2136

Complete contact information is available at: https://pubs.acs.org/10.1021/acs.iecr.5c03286

Notes

The authors declare no competing financial interest.

■ ACKNOWLEDGMENTS

The authors gratefully acknowledge financial support from the National Key Research and Development Program of China (2024YFC3909801), Guizhou Phosphate Chemical Group, and China Institute for Innovation & Development Strategy.

■ REFERENCES

(1) Gong, H.; Yin, Y.; Chen, Z.; Zhang, Q.; Tian, X.; Wang, Z.; Wang, Y.; Cui, Z. A Dynamic Optimization of Soil Phosphorus Status Approach Could Reduce Phosphorus Fertilizer Use by Half in China. *Nat. Commun.* **2025**, *16* (1), 976.

(2) Chavkin, T. A.; González, L. D.; Cansino-Loeza, B.; Larson, R. A.; Pfleger, B. F.; Zavala, V. M. Codesign of Cyanobacteria Mutant Strains and Processes for Phosphorus Recovery from Livestock Wastewater. *ACS Sustain. Chem. Eng.* **2025**, *13* (7), 2672−2682.

(3) Yang, H.; Zhang, H.; Lu, J.; Cui, Y.; Wang, Y.; Wang, X.; Xue, J.; Cao, H. Advanced Magnetic Adsorbents for Enhanced Phosphorus and Fluoride Removal from Wastewater: Mechanistic Insights and Applications. *Sep. Purif. Technol.* **2025**, *353*, 128195.

(4) Cheng, W.; Zhu, Y.; Shao, J.; Zhang, W.; Wu, G.; Jiang, H.; Hu, J.; Huang, Z.; Yang, H.; Chen, H. Mitigation of Ultrafine Particulate Matter Emission from Agricultural Biomass Pellet Combustion by the Additive of Phosphoric Acid Modified Kaolin. *Renew. Energy* **2021**, *172*, 177−187.

(5) Xu, D.; Zhong, B.; Wang, X.; Li, X.; Zhong, Y.; Yan, Z.; Yang, J.; Li, X.; Wang, Y.; Zhou, X. The Development Road of Ammonium Phosphate Fertilizer in China. *Chin. J. Chem. Eng.* **2022**, *41*, 170−175.

(6) Tuominen, M.; Karp, H. J.; Itkonen, S. T. Phosphorus-Containing Food Additives in the Food Supply—an Audit of Products on Supermarket Shelves. *J. Renal Nutr.* **2022**, *32* (1), 30−38.

(7) Ricciardulli, A. G.; Wang, Y.; Yang, S.; Samorì, P. Two-Dimensional Violet Phosphorus: A p-Type Semiconductor for (Opto)Electronics. *J. Am. Chem. Soc.* **2022**, *144* (8), 3660−3666.

(8) Zhang, Y.; Rui, X.; Tang, Y.; Liu, Y.; Wei, J.; Chen, S.; Leow, W. R.; Li, W.; Liu, Y.; Deng, J.; Ma, B.; Yan, Q.; Chen, X. Wet-Chemical Processing of Phosphorus Composite Nanosheets for High-Rate and High-Capacity Lithium-Ion Batteries. *Adv. Energy Mater.* **2016**, *6* (10), 1502409.

(9) Luo, X.; Elrys, A. S.; Zhang, L.; Ibrahim, M. M.; Liu, Y.; Fu, S.; Yan, J.; Ye, Q.; Wen, D.; Hou, E. The Global Fate of Inorganic Phosphorus Fertilizers Added to Terrestrial Ecosystems. *One Earth* **2024**, *7* (8), 1402−1413.

(10) Scholz, R. W.; Wellmer, F.-W.; Mew, M.; Steiner, G. The Dynamics of Increasing Mineral Resources and Improving Resource Efficiency: Prospects for Mid- and Long-Term Security of Phosphorus Supply. *Resour. Conserv. Recycl.* **2025**, *213*, 107993.

(11) Zhu, G.; Yang, Y.; He, L.; Li, H.; Meng, Z.; Zheng, G.; Li, F.; Su, X.; Xi, B.; Li, Z. Novel Synergistic Process of Impurities Extraction and Phophogypsum Crystallization Control in Wet-Process Phosphoric Acid. *ACS Omega* **2023**, *8* (31), 28122−28132.

(12) Becker, P. *Phosphates and Phosphoric Acid: Raw Materials, Technology, and Economics of the Wet Process*; Marcel Dekker, Inc, 1989.

(13) Fang, K.; Xu, L.; Yang, M.; Chen, Q. One-Step Wet-Process Phosphoric Acid by-Product CaSO4 and Its Purification. *Sep. Purif. Technol.* **2023**, *309*, 123048.

(14) Ma, H.; Feng, X.; Zeng, B. Self-Anticorrosion for the Combustion Tower of Heat Recovered Thermal Process Phosphoric Acid Production. *Process Saf. Environ. Protect.* **2018**, *118*, 330−347.

(15) Klugh, B. G. Thermal Production of Phosphoric Acid. *Ind. Eng. Chem* **1932**, *24* (4), 371−374.

(16) Zhang, P. Comprehensive Recovery and Sustainable Development of Phosphate Resources. *Procedia Eng.* **2014**, *83*, 37−51.

(17) Belboom, S.; Szöcs, C.; Léonard, A. Environmental Impacts of Phosphoric Acid Production Using Di-Hemihydrate Process: A Belgian Case Study. *J. Clean Prod.* **2015**, *108*, 978−986.

(18) Atanasova, L. G. Effect of Phosphate Rock Quality on the Efficiency of Phosphoric Acid Production. *Oxid. Commun.* **2015**, *38* (1), 201−209.
(19) Sınırkaya, M.; Özer, A. K.; Gülaboglu, M. S. Investigation of the Changes of P2O5 Content of Phosphate Rock during Simultaneous Calcination/Sulfation. *Powder Technol.* **2011**, *211* (1), 72−76.
(20) Soussi-Baatout, A.; Brahim, K.; Khattech, I.; Kamoun, L.; Jemal, M. Thermochemical and Kinetic Investigations of the Phosphoric Attack of Tunisian Phosphate Ore. *J. Therm Anal Calorim.* **2018**, *131* (3), 3121−3132.
(21) Zhao, Y.; Li, X.; Yu, J.; Li, C.; Ruan, Y.; Abbas, M. A.; Chi, R. Migration and Transformation Behaviors of Phosphorus and Associated Elements in Wet-Process Phosphoric Acid: Acidolysis Process and Mechanism Study. *J. Environ. Chem. Eng.* **2025**, *13* (3), 116327.
(22) Ren, B.; Wang, H.; Xu, D.; Yang, X.; Zhang, Z. Dissolution Behavior and Kinetics of the Phosphorus−Potassium Associated Ore during Phosphoric Acid Leaching. *Ind. Eng. Chem. Res.* **2022**, *61* (50), 18327−18340.
(23) Abutayeh, M.; Campbell, S. W. Predicting the Citrate Soluble Loss of the Dihydrate Process. *Ind. Eng. Chem. Res.* **2009**, *48* (18), 8670−8677.
(24) Bouchkira, I.; Benjelloun, S.; Khamar, L.; Latifi, A. M. Thermodynamic Modeling and Parameter Estimability Analysis of a Wet Phosphoric Acid Process with Impurities. *Fluid Phase Equilib.* **2023**, *564*, 113594.
(25) Tadayyon, A.; Arifuzzaman, S. M.; Rohani, S. Reactive Crystallization of Brushite under Steady State and Transient Conditions: Modeling and Experiment. *Ind. Eng. Chem. Res.* **2003**, *42* (26), 6774−6785.
(26) Oliveira, C.; Ferreira, A.; Rocha, F. Dicalcium Phosphate Dihydrate Precipitation: Characterization and Crystal Growth. *Chem. Eng. Res. Des.* **2007**, *85* (12), 1655−1661.
(27) Dorozhkin, S. V. Fundamentals of the Wet-Process Phosphoric Acid Production. 2. Kinetics and Mechanism of CaSO4·0.5H2O Surface Crystallization and Coating Formation. *Ind. Eng. Chem. Res.* **1997**, *36* (2), 467−473.
(28) Dorozhkin, S. V. Dissolution Kinetics of Single Fluoroapatite Crystals in Phosphoric Acid Solution under the Conditions of the Wet-Process Phosphoric Acid Production. *J. Prakt. Chem.-Chem.* **1996**, *338* (7), 620−626.
(29) Joao, S.; Durand, A.; Schrevens, O. Plant Operability Optimization through Dynamic Simulation, a Case Study Focused on Phosphoric Acid Concentration Unit. *Procedia Eng.* **2016**, *138*, 378−389.
(30) Elmisaoui, S.; Benjelloun, S.; Chkifa, M. A.; Latifi, A. M. Surrogate Model Based on Hierarchical Sparse Polynomial Interpolation for the Phosphate Ore Dissolution. *Comput. Chem. Eng.* **2023**, *173*, 108174.
(31) Elmisaoui, S.; Latifi, A. M.; Khamar, L.; Salouhi, M. Shrinking Core Approach in the Modelling and Simulation of Phosphate Ore Acidulation. *Chem. Eng. Trans.* **2021**, *86*, 871−876.
(32) Bouchkira, I.; Latifi, A. M.; Khamar, L.; Benjelloun, S. Modeling and Multi-Objective Optimization of the Digestion Tank of an Industrial Process for Manufacturing Phosphoric Acid by Wet Process. *Comput. Chem. Eng.* **2022**, *156*, 107536.
(33) Dai, M.; Yang, H.; Wang, J.; Yang, F.; Zhang, Z.; Yu, Y.; Liu, G.; Feng, X. Energetic, Economic and Environmental (3E) Optimization of Hydrogen Production Process from Coal-Biomass Co-Gasification Based on a Novel Method of Ordering Preference Targeting at Bi-Ideal Average Solutions (OPTBIAS). *Comput. Chem. Eng.* **2023**, *169*, 108084.
(34) Dai, M.; Yang, F.; Zhang, Z.; Liu, G.; Feng, X. Energetic, Economic and Environmental (3E) Multi-Objective Optimization of the Back-End Separation of Ethylene Plant Based on Adaptive Surrogate Model. *J. Clean Prod.* **2021**, *310*, 127426.
(35) Cho, H. J.; Yeo, Y.-K.; Park, W. H.; Moon, B. K. Modeling and Simulation of a Wet Hemihydrate Phosphoric Acid Process. *Korean J. Chem. Eng.* **1996**, *13* (6), 585−595.
(36) Bojarski, A. D.; Guillén-Gosálbez, G.; Jiménez, L.; Espuña, A.; Puigjaner, L. Life Cycle Assessment Coupled with Process Simulation under Uncertainty for Reduced Environmental Impact: Application to Phosphoric Acid Production. *Ind. Eng. Chem. Res.* **2008**, *47* (21), 8286−8300.
(37) Cheng, H.-T.; Koc, L.; Harmsen, J.; Shaked, T.; Chandra, T.; Aradhye, H.; Anderson, G.; Corrado, G.; Chai, W.; Ispir, M., et al. Wide & Deep Learning for Recommender Systems. In *Proceedings of the 1st Workshop on Deep Learning for Recommender Systems*; DLRS: New York, NY, USA, 2016; pp. 7−10. .
(38) Zhang, Z.; Song, X.; Zeng, Y.; Li, J.; Nie, Y.; Zhu, M.; Chen, J.; Wang, L.; Xiao, X. Feasible path SQP algorithm for simulation-based optimization surrogated with differentiable machine learning models. *arXiv* **2025**. http://arxiv.org/abs/2501.17495.
(39) Ma, Y.; Zhang, N.; Li, J.; Cao, C. Optimal Design of Extractive Dividing-Wall Column Using an Efficient Equation-Oriented Approach. *Front. Chem. Sci. Eng.* **2021**, *15* (1), 72−89.
(40) Ma, Y.; Gao, X.; Liu, C.; Li, J. Improved SQP and SLSQP Algorithms for Feasible Path-Based Process Optimisation. *Comput. Chem. Eng.* **2024**, *188*, 108751.

https://doi.org/10.1021/acs.iecr.5c03286
Ind. Eng. Chem. Res. 2025, 64, 24138−24155